Stem Cell Reports
Article
ISSCR
OPEN ACCESS

SMAD3 mediates the specification of human induced pluripotent stem cell-derived epicardium into progenitors for the cardiac pericyte lineage

Yutaro Miyoshi,[1,3,5] Antonio Lucena-Cacace,[1,4,5,*] Yu Tian,[1,2] Yasuko Matsumura,[1] Kanae Tani,[1,2] Misato Nishikawa,[1] Megumi Narita,[1] Takeshi Kimura,[3] Koh Ono,[3] and Yoshinori Yoshida[1,6,*]
[1]Center for iPS Cell Research and Application, Kyoto University, Kyoto 606-8507, Japan
[2]Graduate School of Medicine, Kyoto University, Kyoto 606-8501, Japan
[3]Department of Cardiovascular Medicine, Graduate School of Medicine, Kyoto University, Kyoto 606-8507, Japan
[4]Present address: Premium Research Institute for Human Metaverse Medicine (WPI-PRIMe), Osaka University, Suita 565–0871, Japan.
[5]These authors contributed equally
[6]Lead contact
*Correspondence: a.lucena.prime@osaka-u.ac.jp (A.L.-C.), yoshinor@cira.kyoto-u.ac.jp (Y.Y.)
https://doi.org/10.1016/j.stemcr.2024.08.008

SUMMARY

Understanding the molecular mechanisms of epicardial epithelial-to-mesenchymal transition (EMT), particularly in directing cell fate toward epicardial derivatives, is crucial for regenerative medicine using human induced pluripotent stem cell (iPSC)-derived epicardium. Although transforming growth factor β (TGF-β) plays a pivotal role in epicardial biology, orchestrating EMT during embryonic development via downstream signaling through SMAD proteins, the function of SMAD proteins in the epicardium in maintaining vascular homeostasis or mediating the differentiation of various epicardial-derived cells (EPDCs) is not yet well understood. Our study reveals that TGF-β-independent SMAD3 expression autonomously predicts epicardial cell specification and lineage maintenance, acting as a key mediator in promoting the angiogenic-oriented specification of the epicardium into cardiac pericyte progenitors. This finding uncovers a novel role for SMAD3 in the human epicardium, particularly in generating cardiac pericyte progenitors that enhance cardiac microvasculature angiogenesis. This insight opens new avenues for leveraging epicardial biology in developing more effective cardiac regeneration strategies.

INTRODUCTION

During cardiac development, the epicardium plays an essential role in the establishment of blood vessels within the heart, a process referred to as coronary angiogenesis (Olivey and Svensson, 2010). The epicardium gives rise to specialized cells known as epicardial-derived cells (EPDCs) (Smits et al., 2018), which contribute significantly to the development of the coronary vasculature (Lim, 2021). These EPDCs possess the remarkable ability to differentiate into various cell types through distinct cell fate signaling pathways that determine cell lineage decisions (Gittenberger-de Groot et al., 2010). These cell types include vascular smooth muscle cells (Iyer et al., 2015), endothelial cells (Quijada et al., 2021), and fibroblasts (Fang et al., 2016), some of which will form the cardiac vasculature. Moreover, some EPDCs can secrete growth factors and signaling molecules that act as potent stimulants for angiogenesis in cardiac repair, fostering the establishment of a functional vasculature (Volz et al., 2015).

Upon cardiac injury, the epicardium swiftly responds by initiating a process known as epicardial activation (van Wijk et al., 2012). In this scenario, activated epicardial cells proliferate and migrate toward the injured site. These cells secrete growth factors, most notably vascular endothelial growth factor (VEGF), which significantly promotes angiogenesis—an essential part of the cardiac healing process (Chung et al., 2015).

Crucial to this process is epicardial epithelial-to-mesenchymal transition (EMT), which serves as a fundamental mechanism for generating EPDCs (Streef and Smits, 2021). This transition is broadly mediated by transforming growth factor β (TGF-β) signaling via structured responses in coordination with phosphorylated SMAD protein cascades (Sridurongrit et al., 2008). The mechanisms of EMT that operate independently of the canonical TGF-β pathway, however, remain largely unexplored. While the SMAD-mediated epicardial EMT is well understood in a global context, with a primary focus on well-represented EPDCs such as cardiac fibroblasts and smooth muscle cells, it is essential to gain a comprehensive understanding of the intricate mechanisms that underlie epicardial EMT-mediated angiogenesis. This knowledge is critical for devising therapeutic strategies aimed at enhancing cardiac repair and recovery following injury.

Human induced pluripotent stem cells (hiPSCs) (Takahashi and Yamanaka, 2006; Takahashi et al., 2007) have revolutionized the field of regeneration and development by providing an accurate model to recreate the biogenesis of challenging-to-study tissues, such as the human epicardium (Witty et al., 2014). Recently, researchers have successfully differentiated hiPSCs into high-quality epicardial cells, thereby opening avenues for exploring epicardial functionality (Bao et al., 2016; Junghof et al., 2022).

In this context, we have utilized hiPSC-derived epicardium to recreate epicardiogenesis *in vitro* and elucidate

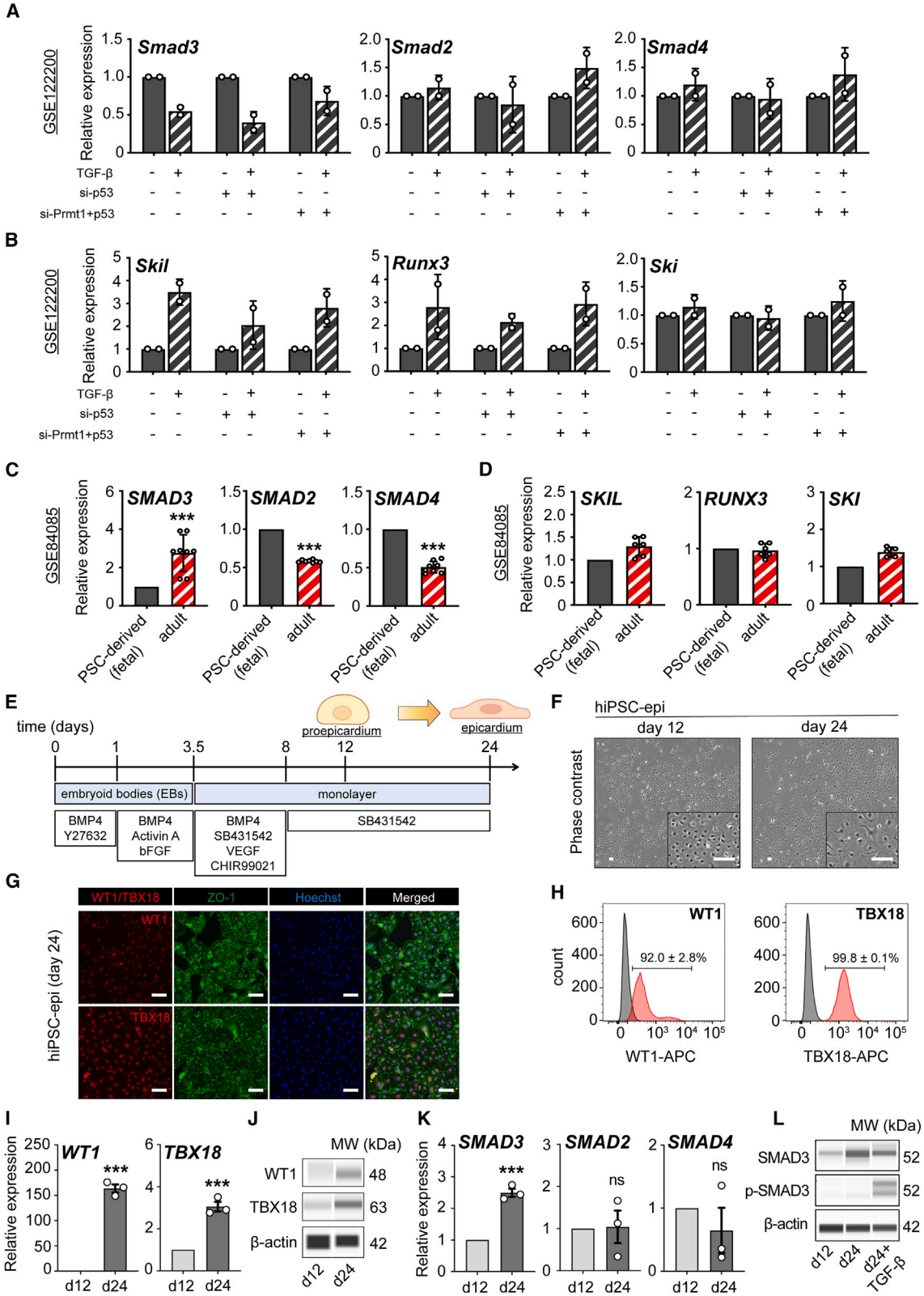

(legend on next page)

the role of SMAD proteins in conditioning epicardial EMT during cell fate decisions. Notably, our findings have unveiled numerous TGF-β-independent functions of SMAD3 in epicardial biology and the priming of cell fate toward angiogenic responses. SMAD3 expression emerged as an independent predictor of successful epicardial differentiation, from the pro-epicardial stage to the full establishment of the fetal program. More importantly, loss of SMAD3 in the fetal epicardium led to a disruption in the epicardial program, initiating an EMT decoupled from TGF-β and SMAD3 phosphorylation. Consequently, this resulted in a pro-angiogenic cell pool enriched in neural/glial antigen 2 (NG2), CD105, CD13, and CD248-expressing cells—functioning as cardiac pericyte progenitor cells (Alex et al., 2022; 2023). These cells exhibited enhanced functionality in supporting primary endothelial cells and promoting increased proliferation of hiPSC-derived ventricular cardiomyocytes.

These findings shed light on novel SMAD3 functions within the human epicardium, endorsing its regenerative and TGF-β-independent capabilities. Furthermore, our research paves the way for the development of engineered epicardial tissues (EETs) primed for enhanced angiogenesis and vascular regeneration—an exciting prospect in the field of cardiac regeneration and tissue engineering.

RESULTS

TGF-β-independent expression of SMAD3 autonomously predicts the development of epicardial cells from induced pluripotent stem cells

To understand the expression dynamics of SMAD genes during TGF-β induction, we first retrospectively analyzed publicly available RNA sequencing (RNA-seq) data (GSE122200) with relevant transcriptomic profiling on epicardial EMT in a mouse epicardial cell line (MEC1). Whereas *Smad2* and *Smad4* showed none to mild transcriptomic upregulation, *Smad3* levels showed a consistent downregulation tendency regardless of the genetic background on the regulatory epicardial EMT axis involving p53-PRMT1, suggesting that despite phospho-Smad3 levels are canonically increased during the onset of the EMT, total gene expression downregulated, indicating an uncoupled TGF-β response with biological implications to be elucidated (Figure 1A). Elevation of some of the TGF-β/SMAD target genes regulating gene expression in the canonical response to EMT initiation was confirmed by the upregulated expression of *Skil*, *Runx3*, and *Ski* (Figure 1B).

Next, to contextualize the expression dynamics of the SMAD genes during epicardial development and maturation, we systemically analyzed the GSE84085 dataset in a differential expression context from pluripotent stem cell (PSC)-derived epicardium compared to donor samples from freshly isolated human adult epicardium. Remarkably, only *SMAD3* mRNA expression showed a significant upregulation in the adult samples compared to fetal PSC-derived samples (Figure 1C), indicating that SMAD3 expression is correlative to the degree of maturation of the tissue in a context of inactive EMT and TGF-β blockage, as indicated by the unchanged expression of SMAD targets (Figure 1D).

Next, in order to understand how SMAD3 expression influences the development and maturation of the human embryonic epicardium, we conducted a systematic study on SMAD gene expression dynamics using hiPSCs to create epicardial-like cells.

Figure 1. Characterization of SMAD gene expression dynamics in epicardial biology using mouse, human, and hiPSC-derived cellular platforms

(A and B) Retrospective analysis using dataset GSE122200 to examine changes in *Smad3*, *Smad2*, and *Smad4* (A) and *Skil*, *Runx3*, and *Ski* (B) in response to TGF-β in MEC1 genetic backgrounds with silenced p53 or both Prmt1 and p53.

(C and D) Retrospective analysis of dataset GSE84085 comparing gene expression of *SMAD3*, *SMAD2*, and *SMAD4* (C) and *SKIL*, *RUNX3*, and *SKI* (D) between human pluripotent stem cell (hPSC)-derived fetal epicardial cells and adult epicardium.

(E) Schematic workflow for the differentiation of epicardial cells from human induced pluripotent stem cells (hiPSCs).

(F) Phase contrast images displaying the cobblestone-like morphology of hiPSC-derived epicardial cells (EPI cells) at day 12 and day 24.

(G) Immunocytochemistry results for WT1, TBX18, and ZO-1 in EPI cells at day 24.

(H) Flow cytometry-derived histograms for WT1 and TBX18 expression with positive ratio in EPI cells at day 24 (red), with gray indicating the unstained control ($n = 3$; mean ± standard error of the mean [SEM]).

(I) Quantitative reverse-transcription PCR (qRT-PCR) analysis showing upregulation of *WT1* and *TBX18* through epicardial induction from day 12 to day 24 ($n = 3$; $^{***}p < 0.001$).

(J) Protein analysis for WT1 and TBX18 expression at day 12 and day 24.

(K) qRT-PCR analysis indicating the transition of *SMAD3*, *SMAD2*, and and *SMAD4* at day 12 and day 24 ($n = 3$; $^{***}p = 0.0003$; ns, not significant).

(L) Western blot analysis of total and phosphorylated SMAD3 at day 12, day 24, and a positive control (day 24+TGF-β for 1 h). All error bars represent SEM; the graph plots are derived from experimental replicates, obtained from independent batches; statistical analysis was performed using a two-sided unpaired Student's t test; scale bars equal 100 μm, unless otherwise indicated; see also Figure S1.

We initiated the differentiation process by generating epicardial-like cells from hiPSCs (referred to as EPI cells). This was achieved by exposing the cells to Activin A and BMP4, leading to the formation of cardiac mesoderm over the course of days 1–3.5. Subsequently, we induced the specification of epicardial fate by activating the WNT signaling pathway from day 3.5 to day 8. To maintain the characteristic features of epicardial cells and enable the long-term culture of EPI cells without spontaneous differentiation, we inhibited TGF-β signaling using SB431542 starting from days 3.5 (Figure 1E). These cells exhibited the typical cobblestone-like morphology expected by day 24 of differentiation (Figure 1F). Notably, by day 24, EPI cells expressed nuclear WT1 and TBX18, which was confirmed through immunofluorescence co-staining with ZO1 (Figure 1G) and flow cytometry (Figure 1H). We further revealed the upregulation of key markers of epicardial cells, such as WT1 and TBX18, during the differentiation process at both the bulk mRNA level (Figure 1I) and total protein level (Figures 1J and S1A). Finally, we confirmed that only SMAD3 showed a steady progressive expression from the pro-epicardial stage (day 12) to the fetal stage (day 24) (Figures 1K and S1B) in the context of inactive EMT, peaking on this day, and maintaining stable long-term expression with no activation of phosphorylated SMAD3 over time (Figures 1L, S1A, S1C, and S1D). hiPSC-derived epicardial monolayers expressed higher SMAD3 levels than their undifferentiated, pluripotent counterparts (hiPSCs) (Figure S1E). The removal of SB431542 led to a time-dependent loss of epicardial identity, which was irreversible; however, no short-term decrease in SMAD3 was observed. This indicates that the time-dependent increase in SMAD3 within the epicardial lineage was specific to lineage specification and not a compensatory regulation driven by TGF-β inhibitory conditions (Figures S1F and S1G).

Altogether, our data indicate that SMAD3 has TGF-β-independent contributions to epicardial biology and could represent an independent predictor of epicardial maturity.

Next, we wanted to evaluate the specific responses of SMAD3 expression in the context of epicardial EMT onset initiated by TGF-β. To that end, we treated hiPSC-derived epicardium at day 24 with 5 ng/mL of TGF-β for 72 h (Figure 2A) and then, we evaluated gene and protein expression at the endpoint, where epicardial monolayers had visibly undergone a morphological transition to EPDCs (Figure 2B). We confirmed the transcriptomic departure from the epicardial fate by the loss of *WT1* and *TBX18* (Figure 2C). Given the developmental-driven changes in transcriptomics depending on cell types, we evaluated three different housekeeping controls and confirmed GAPDH as the preferred one for downstream analyses (Figure S2A). This loss of expression in epicardial markers is consistent with the widely characterized cadherin switch during EMT initiation (Kang and Massagué, 2004; Loh et al., 2019) (Figure 2D). We then confirmed the significant expression of some key EPDC markers *ACTA2*, *CNN1*, *PDGFRA*, and *TAGLN*, both at mRNA and protein levels (Figures 2E, 2F, and S2B). Finally, while we observed unchanged expression in SMAD genes (Figure 2G), a mild decrease in total SMAD3 was noted, as expected via TGF-β-induced ubiquitination mechanisms (Figures 2H and S2B). Importantly, we confirmed an increase in phospho-SMAD3, consistent with a TGF-β-dependent response (Figures 2H and S2B).

SMAD3 overexpression maintains a functional state in fetal epicardial cells without independently promoting either EMT or epicardial maturation

To investigate the role of SMAD3 in epicardial differentiation and maturation, we conducted a 7-day forced expression experiment in day 24 hiPSC-derived epicardial monolayers using a lentivirus expression system (Figure 3A). Following successful transcriptional overexpression confirmation of total SMAD3 and its phosphorylation capacity upon TGF-β treatment (Figures 3B, 3D, and S3A–S3C), we monitored the epicardial morphology throughout the experiment. Interestingly, we did not observe any significant morphological changes either during the initial days of overexpression or at the endpoint (Figure 3C).

We found unchanged expression levels of epicardial markers such as *WT1*, *TBX18*, *ALDH1A2*, and *BNC1*, indicating no perturbation in epicardial identity (Figure 3E). Although we confirmed consistent protein expression patterns for WT1 and TBX18 (Figure 3F), several EMT markers (*CDH1*, *SNAI1*, *SNAI2*) remained unchanged, while *CDH2* and *ZEB1* showed mild upregulation with no observed morphological changes (Figures 3G and S3D). These changes may reflect the effects of SMAD3 overexpression, but they are incomplete as an EMT phenotype. This suggests that SMAD3-driven *CDH2* and *ZEB1* upregulation could contribute to greater tissue homeostasis in overexpression.

Subsequently, we investigated the markers associated with epicardial maturation—defined by a quiescent tissue with lost EMT functions—and found no significant alterations in *UPK3B*, *MSLN*, *ITLN1*, *EFEMP1*, and *C3* (Du et al., 2023; Knight-Schrijver et al., 2022) (Figure 3H).

Since SMAD3 protein levels are relatively constant from day 24 onward, we also performed SMAD3 overexpression on day 12 monolayers to avoid the peak expression time point. However, we did not find any upregulation in epicardial maturation markers (Figures S3E–S3G) indicative of epicardial quiescence or loss of EMT functionality, as cells remained proliferative and responsive to TGF-β. This

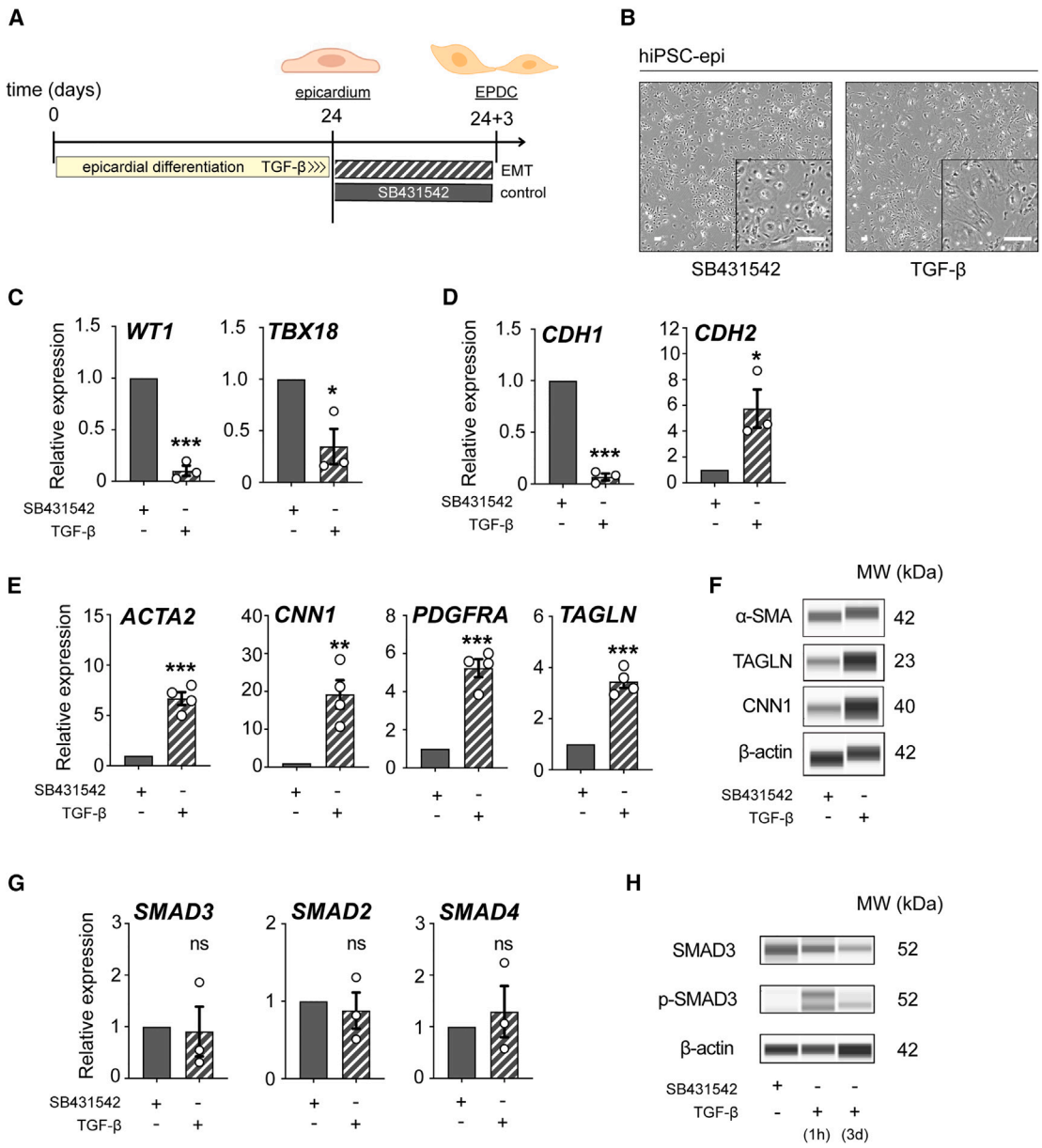

Figure 2. SMAD3 expression dynamics during EMT in hiPSC-derived epicardial monolayers

(A) Description of the experimental workflow for epithelial-to-mesenchymal transition (EMT) induction using TGF-β and the control agent SB431542.

(B) Observations of morphological differences in hiPSC-derived EPI cells treated with TGF-β and SB431542 for 3 days, post day 24.

(C and D) Comparative qRT-PCR analysis of epicardial markers (*WT1* and *TBX18*) (C) and genes *CDH1* and *CDH2* (D) in cells treated with TGF-β versus SB431542 treatment ($n = 3$; $^{*}p < 0.05$, $^{***}p < 0.001$).

(E) qRT-PCR analysis comparing the expression of epicardial-derived cell (EPDC) markers (*ACTA2*, *CNN1*, *PDGFRA*, and *TAGLN*) between TGF-β and SB431542 treatments ($n = 4$; $^{**}p = 0.0028$, $^{***}p < 0.001$).

(F) Western blot (Wes) analysis of EPDC markers (α-SMA, CNN1, and TAGLN) comparing TGF-β and SB431542 treatments.

(G) Comparison of qRT-PCR results for *SMAD3*, *SMAD2*, and *SMAD4* between cells treated with TGF-β and SB431542 ($n = 3$; ns, not significant).

(H) Western blot analysis of total and phosphorylated SMAD3 in cells treated with TGF-β versus SB431542 (TGF-β treatment for 1 h is used as a positive control). All error bars represent SEM; the graph plots are derived from experimental replicates, obtained from independent batches; statistical analysis was performed using a two-sided unpaired Student's t test; scale bars equal 100 μm, unless otherwise indicated; see also Figure S2.

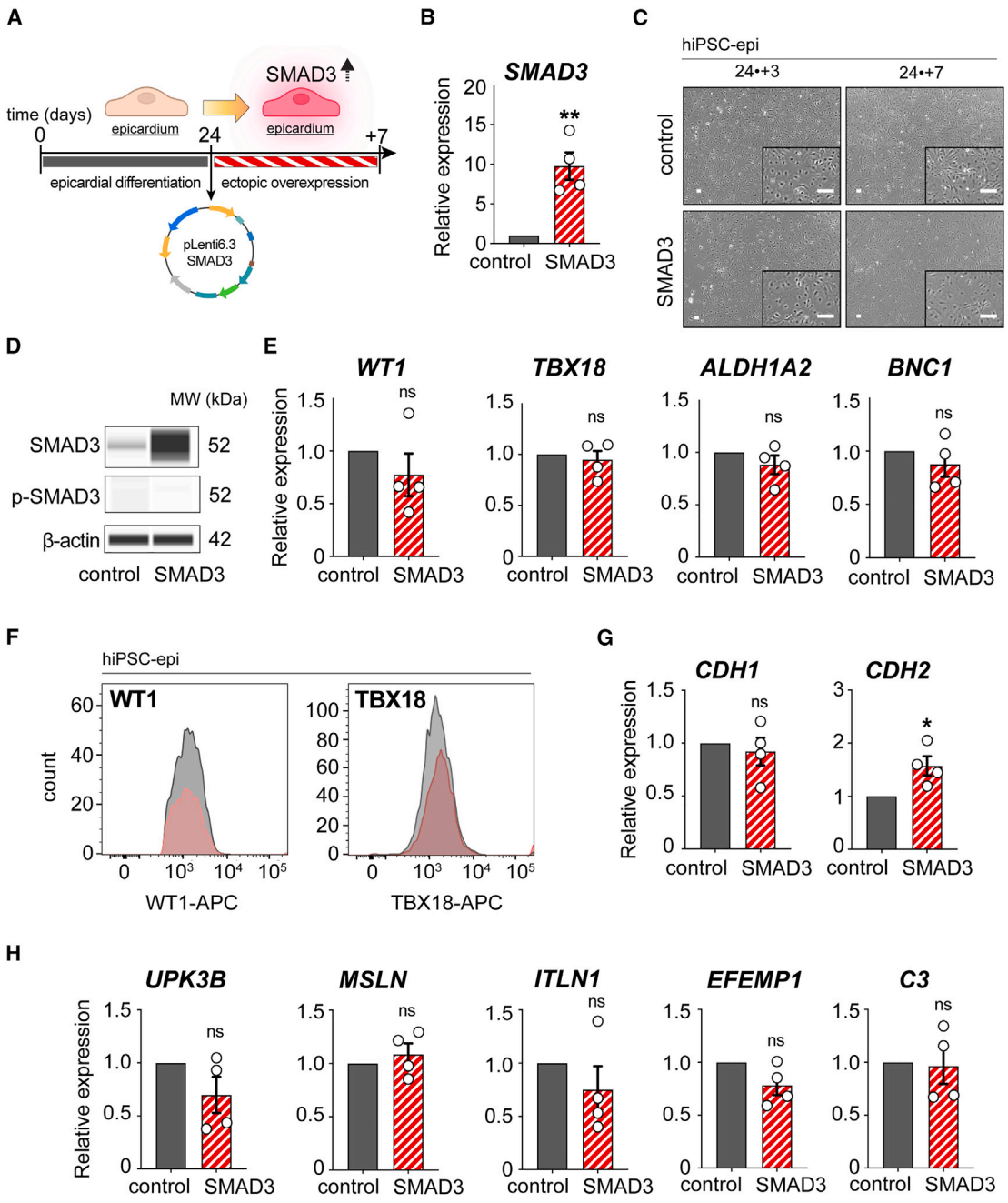

Figure 3. Characterization of hiPSC-derived epicardium during ectopic SMAD3 overexpression

(A) Description of the experimental process for inducing SMAD3 overexpression using a lentivirus.

(B) Validation of *SMAD3* overexpression through qRT-PCR analysis ($n = 4$; $^{**}p = 0.0023$).

(C) Time-lapse phase contrast imaging of hiPSC-derived EPI cells at 3 days and 7 days following SMAD3 overexpression.

(D) Western blot analysis of total and phosphorylated SMAD3 in SMAD3-overexpressing EPI cells.

(E) qRT-PCR analysis of epicardial markers, including *WT1*, *TBX18*, *ALDH1A2*, and *BNC1* ($n = 4$; ns, not significant).

(F) Flow cytometry assessment of epicardial markers WT1 and TBX18, showing no significant difference between SMAD3 overexpression (red) and control (gray).

(G) qRT-PCR analysis for genes *CDH1* and *CDH2* ($n = 4$; ns, not significant, $^{*}p = 0.020$).

(legend continued on next page)

suggests that the autonomous expression of SMAD3 alone did not induce epicardial maturation. Therefore, our findings indicate that while sustained SMAD3 expression may signify progress in epicardial specification and maturation, it is insufficient to promote maturation on its own. This implies that epicardial maturation requires a more complex interplay of factors during its developmental process.

Loss of SMAD3 in epicardial cells triggers a poised EMT that leads to the derivation of cardiac pericyte progenitors

To investigate the functional role of SMAD3 in maintaining the epicardial program, we employed a strategy to downregulate SMAD3 expression in day 24 hiPSC-derived epicardial monolayers while maintaining TGF-β blockage (SB431542) to prevent the spontaneous activation of epicardial EMT (Figure 4A). The downregulation of SMAD3 resulted in viable cells (Figure S4A) with noticeable morphological changes with a subset of cells transitioning to an elongated shape and losing the characteristic cobblestone-like morphology, indicative of a shift toward mesenchymal cells (Figure 4B). We confirmed a significant reduction in SMAD3 levels within this cell subset, both at the mRNA and protein levels, 7 days after siRNA expression (Figures 4C, 4D, and S4B). Interestingly, the phosphorylated levels of SMAD3 remained unchanged during these morphological dynamics, suggesting that the cell transition was driven by a direct on-target mechanism of SMAD3 rather than initiating a canonical TGF-β-SMAD pathway-dependent epicardial EMT (Figure 4D).

Further confirmation of the departure from epicardial cells was evident through the loss of epicardial markers WT1, ZO-1, and TBX18 (Figures 4E–4G and S4B). Notably, we observed a steady time-dependent transition in cadherin expression and the upregulation of endpoint EMT activation markers such as *SNAI1*, *SNAI2*, *and ZEB1* at the transcriptional level throughout SMAD3 downregulation, indicating the initiation of EMT (Figure S4C).

To delve deeper into the newly acquired identity of EPDCs, we systematically examined the mRNA expression levels of major epicardial EPDC subtypes, including cardiac fibroblasts, smooth muscle cells, and cardiac pericytes. While markers such as *ACTA2*, *CNN1*, *TAGLN*, and *POSTN*, as well as the EMT axis p53-PRMT1, showed either unchanged or downregulated expression patterns (Figure S4D), we observed significant overexpression of endoglin (CD105) and CSPG4 (NG2) at both the gene expression and protein levels (Figures 4H, 4I, and S4B). Additionally, enhanced protein expression of CD248 and CD13 (Zhu et al., 2022) was confirmed in SMAD3-downregulating cells (Figures 4I and S4B). These are all known markers associated with the cardiac pericyte fate. Protein expression of CD105 (Figure 4J) and NG2 (Figure 4K) in SMAD3-downregulating bulk monolayers was further verified. Quantitative analysis using fluorescence-activated cell sorting revealed that 8.2% of cells expressed CD105, while 12.9% expressed NG2 (Figures 4L, 4M, and S4E), and these data were plotted in their respective histogram plots (Figures 4N and 4O). The modest representation of cardiac pericyte markers at the protein level may indicate a premature developmental stage of cardiac pericyte progenitor cells, with the bulk population transitioning toward the full establishment of this transcriptional lineage landscape.

To expand our understanding, we conducted a comprehensive transcriptional analysis of SMAD3-downregulating cells, focusing on a curated selection of cardiac pericyte markers to confirm that our condition was significantly enriched in *DLK1*, *CD13*, *CD146*, and *CD248*, further supporting the presence of cardiac pericyte hallmarks (Figure 4P). Importantly, to dissociate this phenotype from the TGF-β-driven EPDC differentiation into hiPSC-derived cardiac fibroblasts (iCFs) and smooth muscle cells (iSMCs), we verified that the cell pools resulting from TGF-β and basic fibroblast growth factor (bFGF) treatments do not express either CD248 or NG2, while EPDC markers are highly expressed in differentiation condition toward iCF and iSMC cell fates. This confirms that the enrichment of a cardiac pericyte-like fate is indeed an on-target mechanism driven by SMAD3 downregulation (Figures S4F and S4G). Mechanistically, TGF-β can activate both the ALK1 (activin receptor-like kinase 1) and ALK5 (activin receptor-like kinase 5) pathways. TGF-β signals through a family of serine/threonine kinase receptors, which include type I receptors such as ALK1 and ALK5. While the ALK5 pathway usually activates phospho-SMAD2 and 3, the ALK1 pathway is mainly associated with the activation of phospho-SMAD1, 5, and 9. We confirmed that phospho-SMAD2 does not compensate for the activation of the ALK5 pathway in the absence of phospho-SMAD3 (Figures S5A and S5B). Additionally, we confirmed that the ALK1 pathway is not compensating, neither at the mRNA nor protein levels (Figures S5A, S5C, and S5D). Our data support that the nature of this EMT and the increased expression of CD105 are not caused by the relative activation of either the ALK1 or ALK5 pathways, which are key players in TGF-β-mediated signaling.

(H) qRT-PCR analysis for mature epicardial markers: *UPK3B*, *MSLN*, *ITLN1*, *EFEMP1*, and *C3* ($n = 4$; ns, not significant). All error bars represent SEM; the graph plots are derived from experimental replicates, obtained from independent batches; statistical analysis was performed using a two-sided unpaired Student's t test; scale bars equal 100 μm, unless otherwise indicated; see also Figure S3.

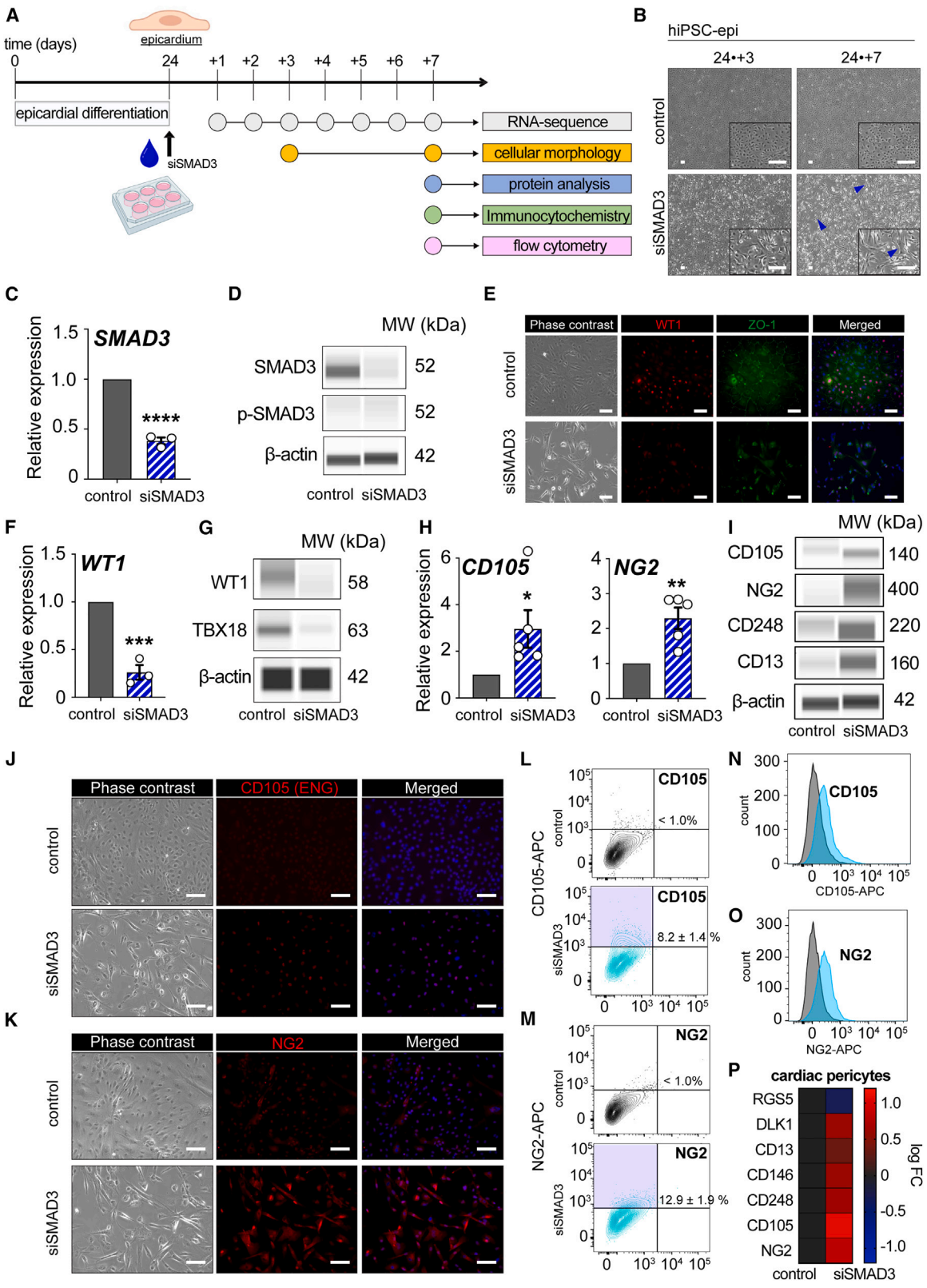

(legend on next page)

We also investigated whether the concurrent downregulation of SMAD3 and TGF-β induction could modify cell fate decisions. While TGF-β led the fate trajectory to produce a pool of cells expressing markers of iSMC and iCF as expected, adding siSMAD3 to the experimental condition included CD105, NG2, CD13, and CD248-expressing cells (progenitors of the cardiac pericyte lineage) in the pool (Figures S5E and S5F). In summary, our findings suggest that the loss of SMAD3 disrupts the embryonic epicardial program, initiating a TGF-β-independent EMT.

SMAD3-downregulating cells signal reparative factors and exhibit pro-angiogenic properties improving functions of primary endothelial cells

To comprehensively understand the cellular functionality of SMAD3-downregulating cells, we conducted whole mRNA sequencing (RNA-seq) to dissect the transcriptomic landscape of these cells in comparison to other known EPDC trajectories, including iSMCs and iCFs. Principal component analysis demonstrated that SMAD3-downregulating cells exhibited distinct transcriptomic profiles compared to other EPDCs (Figure 5A), further confirming their emergence as cardiac pericyte progenitor cells with a unique cellular identity.

Gene Ontology analysis focusing on biological processes unveiled terms related to angiogenesis, wound repair, and the regulation of blood vessels (Figure 5B). As an illustrative example, we generated a heatmap displaying genes associated with the first two terms: (1) positive regulation of angiogenesis and (2) regulation of response to wounding. Notable genes contributing to both processes, such as *CXCL8* and *SERPINE1* for angiogenesis regulation (Hooglugt et al., 2020) and *IL33* and *PLAU* for response to wounding regulation (Yin et al., 2013), were prominently expressed (Figure 5C).

Subsequently, we highlighted a curated selection of genes potentially implicated in cardiac angiogenesis, with a particular emphasis on *CD44*, *VEGFA*, and *PDGFRA* (Figure 5D). CD44, a marker indicative of mesenchymal stemness and heightened pro-angiogenic potential (Zhang et al., 2022), exhibited enhanced expression in SMAD3-downregulating cells (Figures 5E and S6A).

We further examined the temporal expression patterns of candidate genes encoding secreted proteins that could contribute to the regenerative milieu. Notably, we observed increased expression of *SDF-1*, *VEGFA*, angiopoietin-1 (*ANGPT1*), and *IL-6*, suggesting their potential involvement in enhanced functionality within a reparative context (Figure 5F).

To assess the reparative potential of siSMAD3 cells as cardiac pericyte progenitors, we transduced lentiviruses carrying EGFP for monitoring and co-cultured them with a primary cell line of endothelial cells (human aortic endothelial cell [HAEC]) (Figure 5G). *In vitro* endothelial tube formation assays were performed to evaluate endothelial cell functionality. Following optimization of cell ratios (data not shown), we observed a substantial enhancement in the tubule formation capacity of HAEC when co-cultured with siSMAD3 cells after 6 h (Figure 5H), resulting in a significant increase in the number of formed junctions (Figure 5I). Importantly, we observed physical interactions suggestive of cardiac pericyte-like behavior exhibited by siSMAD3 cells as they are closely associated with HAECs (Figures 5J and 5K). Collectively, our data endorse the pro-angiogenic functionality of siSMAD3 cells, potentially attributed to their physical association with endothelial cells, thereby

Figure 4. Loss of SMAD3 in hiPSC-derived epicardium causes EMT toward cardiac pericyte progenitor cells

(A) Overview of the siRNA transfection experiment and subsequent analysis steps.

(B) Phase contrast microscopy images captured on day 27 (day 24 + 3) and day 31 (day 24 + 7) highlighting spindle-like morphology in hiPSC-derived EPI cells with silenced SMAD3, as indicated by blue arrowheads.

(C) Evidence of *SMAD3* downregulation post-siRNA transfection, as shown by qRT-PCR ($n = 3$; $^{****}p < 0.0001$).

(D) Western blot (Wes) analysis revealing a decrease in total SMAD3 levels with no change in phosphorylated SMAD3.

(E) Immunocytochemistry results for WT1 and ZO-1 7 days following siRNA transfection.

(F) Reduction in *WT1* expression due to SMAD3 silencing, as determined by qRT-PCR ($n = 3$; $^{***}p = 0.0006$).

(G) Western blot results showing decreased protein expression of WT1 and TBX18 by SMAD3 silencing.

(H) qRT-PCR analysis for *ENG* (*CD105*) ($n = 5$; $^{*}p < 0.05$) and *NG2* ($n = 5$; $^{**}p < 0.01$).

(I) Western blot analysis indicating increased levels of CD105, NG2, CD248, and CD13 in SMAD3-silenced EPI cells.

(J and K) Immunocytochemistry images for ENG (CD105) (J) and NG2 (K) comparing SMAD3-silenced and control (scramble) EPI cells 7 days after siRNA transfection.

(L and M) Flow cytometry contour plots analyzing CD105 (L) and NG2 (M) expression.

(N and O) Flow cytometry-derived histograms for CD105 expression (N) and NG2 expression (O) (gray represents the unstained control).

(P) Heatmap displaying a curated gene set associated with the cardiac pericyte lineage in cells with downregulated SMAD3 (log fold change). All error bars represent SEM; the graph plots are derived from experimental replicates, obtained from independent batches; statistical analysis was performed using a two-sided unpaired Student's t test; scale bars equal 100 μm, unless otherwise indicated; scrambled siRNA was used as a control; see also Figures S4 and S5.

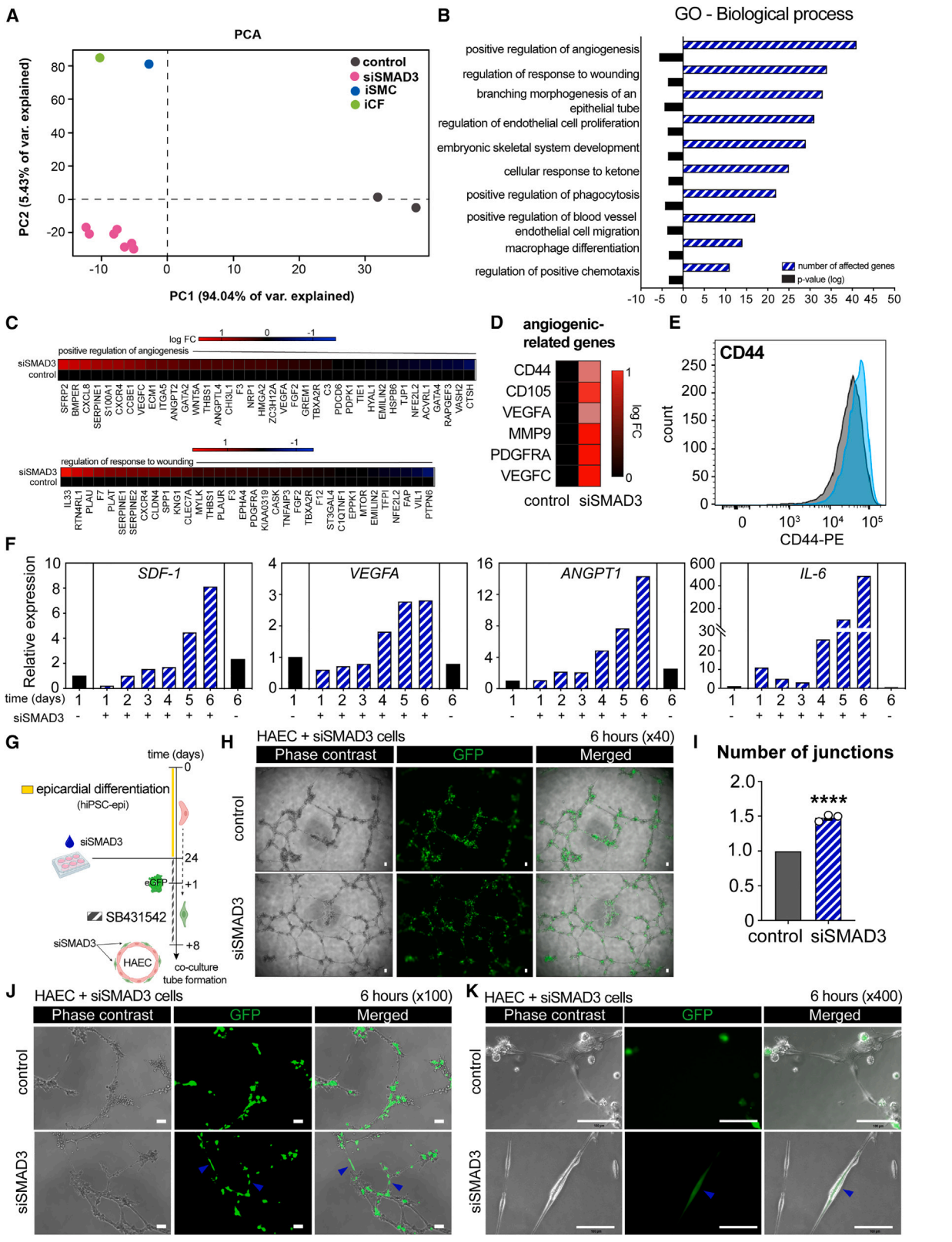

(legend on next page)

improving their overall functionality within a reparative context.

SMAD3-downregulating cells release soluble factors that enhance paracrine-driven proliferative reactivation of hiPSC-derived cardiomyocytes

VEGFA and ANGPT1 are well-known factors that promote angiogenesis and activate proliferative pathways in the functional myocardium following myocardial infarction. Cardiomyocyte proliferation relies, in part, on the CDK6/CCND1 axis. Enhanced expression of CDK6 can induce proliferation in cardiomyocytes, which are typically quiescent and exhibit proliferative arrest, presenting a significant hurdle in cardiac repair (Rhee and Wu, 2018).

To investigate cardiac differentiation, we employed a reporter induced pluripotent stem cell line (FUCCI [fluorescent ubiquitination-based cell cycle indicator]) (Kasamoto et al., 2023) to differentiate ventricular cardiomyocytes (hiPSC-CMs) and monitor the proliferative state of hiPSC-CMs in response to siSMAD3 supernatant (Figure 6A).

Following the epicardial differentiation and ectopic silencing of SMAD3 to divert EMT toward cardiac pericyte progenitor cells, we co-cultured ventricular cardiomyocytes in monolayers (cTnT+) (Figure 6B) with siSMAD3 cell supernatant to observe changes in the proliferative state using the FUCCI system. After 36 h of culture, a noticeable increase in FUCCI-green cells was observed under similar cardiomyocyte cell density (Figures 6C–6E), indicating reactivation of proliferation due to secreted factors present in the supernatant collected from siSMAD3 cells. Notably, gene expression analysis of treated hiPSC-CMs showed increased mRNA expression of fetal cardiac troponin I (TNNI1), possibly indicating the emergence of *de novo* fetal hiPSC-CMs (Figure 6F). There was a significant increase in *CCND1* levels and an upward trend in *CDK4* and *CDK6* mRNA levels, suggesting proliferative activity in hiPSC-CMs (Figure 6F). In addition, protein analysis revealed an increasing tendency of TNNI1, CDK4, and CDK6 (Figures 6G and S6B). Finally, we performed immunodetection analysis (ELISA) in siSMAD3-derived supernatant to identify mechanistically the causative effector of increased hiPSC-CM proliferation. While we failed to detect the difference in secreted SDF-1 or ANGPT1 proteins, we detected a significant upregulation in secreted VEGFA in the supernatant of siSMAD3 EPI cells compared to control hiPSC-derived epicardial monolayers (Figures 6H and S6C). In summary, our findings demonstrate that the siSMAD3 secretome can enhance cardiac proliferation in an extrinsic manner, partially through the paracrine secretion of VEGFA that targets the CDK6/CCND1 axis, partially activating the cell cycle of hiPSC-CMs.

DISCUSSION

Leveraging epicardial EMT mechanisms to guide cell fate decisions in regeneration holds promise as a therapeutic strategy for constructing EETs to repair injured hearts and transplant regenerative cells for myocardial healing (Jackman et al., 2018; Tan et al., 2021). The reconstruction of the human epicardium using induced pluripotent stem cells (iPSCs) has emerged as a compelling approach,

Figure 5. SMAD3-downregulating epicardial cells show pro-angiogenic properties in transcriptomic analysis and functional assay with endothelial cells

(A) Principal component analysis (PCA) plot comparing control hiPSC-derived EPI cells at day 1 and day 7, SMAD3-silenced EPI cells from day 1 to day 7, iPSC-derived smooth muscle cells (iSMCs), and iPSC-derived cardiac fibroblasts (iCFs) (● control, $n = 2$; ● siSMAD3, $n = 7$; ● iSMC, $n = 1$; ● iCF, $n = 1$).

(B) Gene Ontology (GO) analysis focusing on the biological processes of genes upregulated in SMAD3-silenced EPI cells.

(C) Heatmaps illustrating genes that are upregulated and downregulated in SMAD3-silenced EPI cells, specifically those associated with the positive regulation of angiogenesis and regulation of response to wounding, compared with control EPI cells.

(D) Heatmap depicting the upregulation of angiogenic-related genes in SMAD3-silenced EPI cells.

(E) Flow cytometry analysis revealing an increase in CD44 expression in SMAD3-silenced EPI cells (light blue) (gray represents the unstained control).

(F) Time-course upregulation of *SDF-1*, *VEGFA*, *ANGPT1*, and *IL-6* in response to SMAD3 silencing, as observed in RNA sequencing data.

(G) Description of the experimental workflow, including siRNA transfection, EGFP overexpression, and co-culture in an endothelial tube formation assay.

(H) Phase contrast and immunofluorescent imaging of the endothelial tube formation assay at 6 h, comparing co-cultured human aortic endothelial cells (HAECs) with control and SMAD3-silenced EPI cells.

(I) Quantitative analysis showing an increased number of junctions in HAEC when co-cultured with SMAD3-silenced EPI cells ($n = 3$; $^{****}p < 0.0001$).

(J and K) Observation of GFP-positive tubules, indicated by blue arrowheads, exclusively in HAEC co-cultured with SMAD3-silenced EPI cells. All error bars represent SEM; the graph plots are derived from experimental replicates, obtained from independent batches; statistical analysis was performed using a two-sided unpaired Student's t test; scale bars equal 100 μm, unless otherwise indicated; scrambled siRNA was used as a control; see also Figure S6.

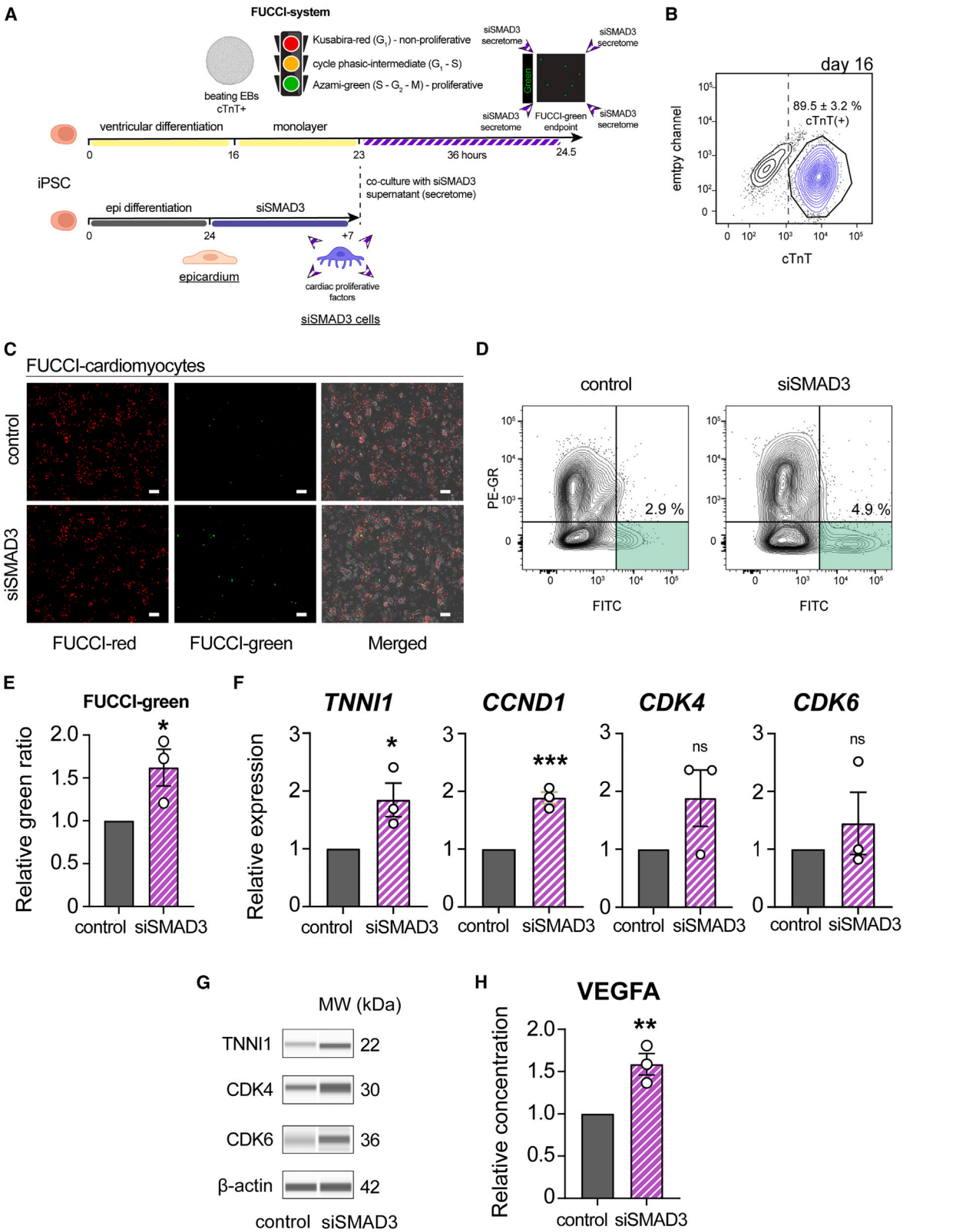

(legend on next page)

reactivating the adult primary tissue from a quiescent state to stimulate *in situ* regeneration involving unknown mechanisms (Suffee et al., 2020).

Our hiPSC-derived epicardium serves as a robust source of cardiac progenitor cells with high plasticity for regenerative phenotypes, as previously demonstrated (Junghof et al., 2022). While the differentiation of human epicardium into EPDCs has been well documented for certain populations like cardiac fibroblasts and vascular smooth muscle cells, it typically involves trigger molecules such as bFGF or TGF-β, a potent inducer of EMT (Whitehead et al., 2022).

TGF-β is a multifunctional cytokine that plays a crucial role in various cellular processes, including cell growth, differentiation, and tissue homeostasis (Tzavlaki and Moustakas, 2020). TGF-β exerts its biological effects by binding to specific cell surface receptors (Heldin and Moustakas, 2016). Two important receptors involved in TGF-β signaling are ALK1 and ALK5 (Goumans et al., 2003). Although our study indicated a potential pathway connection involving endoglin (CD105) expression, which is a significant mediator in the ALK1 pathway (Roman and Hinck, 2017), the loss of SMAD3 had no impact on this pathway. This finding supports the idea that the observed CD105 expression was more likely associated with a new cellular identity rather than being a TGF-β-response element (Rossi et al., 2019). It is increasingly recognized that signaling pathways like TGF-β have pleiotropic effects, and the downstream SMAD protein signaling is highly context dependent (Derynck and Zhang, 2003). It can vary based on the cellular environment, the presence of other signaling molecules, and developmental timing. Our study has unveiled a novel role for SMAD3 in epicardial biology, indicating that SMAD3 expression can independently signify epicardial differentiation and stability over time.

However, SMAD3 overexpression alone appeared insufficient to autonomously induce a maturation phenotype from fetal epicardium. The effects of SMAD3 overexpression in hiPSC-derived epicardial monolayers may exhibit non-linear or biphasic behavior, making it challenging to replicate the physiological expression pattern of SMAD3 during development. Our study suggests that SMAD3 in the human epicardium fulfills a broader spectrum of functions (Dennler et al., 1998).

Cardiac pericytes are crucial for vessel stabilization, angiogenesis, and tissue homeostasis (Quijada et al., 2023). They are known for their transcriptional heterogeneity and can express various markers depending on factors like their location, developmental origin, and specific organ (Avolio et al., 2024).

Common pericyte markers include PDGFRβ (platelet-derived growth factor receptor-beta) and NG2 (also known as CSPG4) (Smyth et al., 2022). However, not all pericytes express both markers simultaneously (Yamazaki and Mukouyama, 2018). Our SMAD3-downregulating cells exhibited no protein expression of PDGFRβ, even though they displayed characteristics of cardiac pericytes in our experimental setup. This variability can be influenced by factors such as the developmental stage or the presence of specific signaling molecules.

Our study suggests that SMAD3-downregulating cells may represent an immature pericyte state with the potential to differentiate into mature pericyte-like cells (Bouacida et al., 2012). During this differentiation process, the expression of pericyte markers may change. As these cells mature and integrate into the cardiac microvasculature, their marker expression may become more pronounced or diversified (Lerman et al., 2018).

A recent study that differentiated cardiac pericytes from hiPSCs (Shen et al., 2023) indicated that exogenous supplementation of PDGF-BB (platelet-derived growth factor BB), primarily secreted by endothelial cells, is necessary to yield PDGFRβ-expressing cells. Since our study primarily focuses on characterizing the autonomous expression of SMAD3 in

Figure 6. Characterization of siSMAD3-derived secretome in hiPSC-CM proliferation

(A) Schematic illustration of the co-culture experiment, involving the treatment of hiPSC-derived cardiomyocytes (hiPSC-CMs) with the secretome derived from siSMAD3 treatment, to monitor cardiomyocyte proliferation using FUCCI (fluorescent ubiquitination-based cell cycle indicator) cells.

(B) Flow cytometry analysis to identify cTnT-positive cells in hiPSC-CMs at differentiation day 16 (n = 3; mean ± SEM).

(C) Fluorescence microscopy to observe FUCCI-red (non-proliferative) and FUCCI-green (proliferative) hiPSC-CMs.

(D) Representative flow cytometry contour plots analyzing FUCCI-green percentage.

(E) FUCCI-green percentage in hiPSC-CMs following treatment with the siSMAD3-derived supernatant compared to control (n = 3; *p = 0.044).

(F) qRT-PCR analysis for *TNNI1*, *CCND1*, *CDK4*, and *CDK6* gene expression in hiPSC-CMs following treatment with the siSMAD3-derived supernatant (n = 3; *p = 0.044, ***p = 0.0010, ns = not significant).

(G) Protein analysis in treated hiPSC-CMs for the detection of TNNI1, CDK4, and CDK6 proteins.

(H) ELISA showing that VEGFA concentration in the supernatant from SMAD3-silenced EPI cells was 49.5 pg/mL, 1.59 times compared to control (n = 3; **p = 0.010). All error bars represent SEM; the graph plots are derived from experimental replicates, obtained from independent batches; statistical analysis was performed using a two-sided unpaired Student's t test; scale bars equal 100 μm, unless otherwise indicated; scrambled siRNA was used as a control; see also Figure S6.

epicardial biology and the specification of cardiac pericyte progenitor cells, without investigating factors secreted by other cardiac cell types, it is possible that PDGF-BB could trigger a pericyte maturation program in SMAD3-downregulating cells.

Angiogenesis is a pivotal process in tissue reconstitution during cardiac repair (Kobayashi et al., 2017; Li et al., 2022), and the human epicardium can assess the extent of damage and the specific cellular response required based on external cues.

Loss of SMAD3 has been linked to various functions related to vascular remodeling (Cobb et al., 2022; Zabini et al., 2018), angiogenesis, and the maintenance of microvascular homeostasis (Feinberg et al., 2004). SMAD transcription factors occupy a central position in a highly adaptable cytokine signaling pathway that remains incompletely understood (Massagué et al., 2005). Angiotensin II can activate the SMAD pathway in vascular smooth muscle cells (Carvajal et al., 2008), similar to the way TGF-β does. It is conceivable that the human epicardium has evolved to preserve a broader spectrum of differentiation capabilities beyond our current knowledge. SMAD3 specifically regulates a differentiation process leading to a pro-angiogenic phenotype (Nakagawa et al., 2004), highlighting its significance in cardiac vascular processes.

SMAD3-downregulating cells exhibited an inherent ability to interact with primary endothelial cells, facilitating enhanced microvasculature formation *in vitro*, mimicking the process of vascular development *in vivo* (Bergers and Song, 2005; Geevarghese and Herman, 2014; Yuan et al., 2016). Our study demonstrated that SMAD3 regulates the secretion of regenerative factors involved in at least two critical processes during cardiac repair: (1) vascular repair and (2) stimulation of functional myocardial regeneration. While our study did not identify the specific secreted factors promoting hiPSC-CM proliferation, promising candidates include SDF-1, VEGFA, and ANGPT1, which are known to stimulate cardiomyocyte proliferation (Chen et al., 2015; Eschenhagen et al., 2017; Lin and Pu, 2014; Renko et al., 2018; Tao et al., 2011). Although a few conceptual studies have shown that cardiomyocytes can re-enter the cell cycle through small molecules or genetic approaches (Kasamoto et al., 2023), our research suggests that EPDCs play a crucial role in cardiac repair by promoting functional myocardial regeneration.

Our experiments using SMAD3-downregulating cell secretome showed a mild increase in FUCCI-green, indicating that cardiomyocyte cell cycle reactivation involves a broader network of genes beyond CDK6/CCND1 (Li et al., 2021; Murganti et al., 2022). This reactivation possibility offers the potential to generate highly engraftable hiPSC-CMs. Proliferative cardiomyocytes can integrate more effectively into host hearts, as demonstrated in a recent study that induced cardiac proliferation using Am80, a retinoic acid receptor agonist (Kasamoto et al., 2023).

In summary, our study sheds light on the manipulation of epicardial EMT, with SMAD3 playing a vital role in the specification and maintenance of the epicardial program independently. The mechanism by which the loss of SMAD3 overrides the effects of SB431542 (Bao et al., 2016) in blocking TGF-β to initiate an alternative epicardial EMT remains unclear, and further research on SMAD3 DNA interactions during epicardiogenesis is warranted. In conclusion, our work defines a biological function of SMAD3 in the epicardial context, opening avenues for the manipulation and therapeutic modulation of the active epicardium for cardiac repair and regeneration. This includes the generation of cardiac pericyte progenitor cells capable of interacting with and promoting *in situ* regeneration of primary tissue, potentially aiding in the recovery of injured myocardium and cardiac microvasculature.

RESOURCE AVAILABILITY

Lead contact

Further information and requests for resources and reagents should be directed to and will be fulfilled by the lead contact, Yoshinori Yoshida (yoshinor@cira.kyoto-u.ac.jp).

Materials availability

All unique and stable reagents generated in this study are available from the lead contact upon completion of a Materials Transfer Agreement.

Data and code availability

All data presented in this study are available within the main text, in the supplemental items file, and can be obtained from the corresponding authors upon request. The RNA-seq data have been deposited in the GEO database under the accession code GSE165450.

EXPERIMENTAL PROCEDURES

Cell lines and culture conditions

We used two hiPSC lines (409B2 and 201B7-FUCCI), both of which were reprogrammed using Yamanaka factors via retroviral methods. Both cell lines were cultured in ReproCell Primate ES cell media supplemented with 4 ng/mL recombinant human bFGF on irradiated MEF feeder cells. In the timing of passage or induction, the feeder layers were eliminated by CTK. Experiments using human iPSCs were approved by the Ethics Committee of Kyoto University.

The human aortic endothelial cell line (ScienCell, # SCR-6100-1) was cultured in endothelial cell medium (ScienCell, # 1001) following the manufacturer's manual.

Regular mycoplasma testing was conducted to avoid contamination for all cell lines.

Cell transfection

We diluted the following Silencer Select siRNAs (Thermo Fisher Scientific) to a 10 μmol/L stock solution: siSMAD3 (Cat #: 4392420, ID: s535081) and negative control (scrambled siRNA) (Cat #: 4390844). For silencing experiments, the cells were seeded to be 60%–70% confluent one day before the transfection. To silence the cells, 10 μL of the siRNA stock and 10 μL of Lipofectamine RNAiMAX reagent were separately diluted in 500 μL of Opti-MEM. These two solutions were mixed and after 15 min incubation at room temperature, the final solution was added dropwise, 500 μL silencing solution into one well of 6-well plate with 2 mL maintenance media. At 24 h after transfection, the media was exchanged and cells were continued to be cultured for 7 days with changing the media containing SB431542 (epicardial maintenance media) every 2–3 days.

Overexpression

For *SMAD3* overexpression, human SMAD3 ORF (NM_001407011.1) was amplified by PCR, subcloned into pENTR-D-TOPO (Invitrogen, #K2400-20), and transferred to pLenti6.3/V5-DEST (Invitrogen, #V533-06), as the protocol instructed (the vector map is shown in Figure S6D). For *EGFP* overexpression, we used control vector in the kit.

The cells were seeded to be 60%–70% confluent one day before the transduction. After optimization of the concentration of lentiviruses, 1.0×10^7 IFU/mL lentiviruses and 4 μg/mL polybrene were transduced to the cells. Thereafter, centrifugation (32°C, 1200 × g, 90 min) was performed to increase transduction efficiency. At 24 h after transduction, the media was exchanged and cells were continued to be cultured for 7 days as aforementioned.

Bioinformatics and RNA-seq

A retrospective analysis of SMAD3 gene expression was conducted using the GSE122200 dataset from GEO for studying EMT dynamics in the mouse epicardium, and GSE84085 for analyzing PSC-derived epicardium and adult primary human epicardium from donors.

For the in-house RNA-seq data generated for this manuscript, normalization was performed using the NOISeq package. The processed data and raw fastq files from this study were submitted to the Gene Expression Omnibus (GEO) under the accession code GSE165450. Further analysis of the raw data was conducted in RStudio.

Gene expression data were read, explored, and pre-processed using the Bioconductor package NOISeq was used for differential expression analysis of RNA-seq. A hierarchical cluster dendrogram was generated using the hclust function from the stats package and the agnes function from the cluster package, with distances assessed by the Manhattan city-block distance algorithm. K-means clustering was performed using the kmeans function. Distance and correlation matrices were computed and plotted using the get_dist and fviz_dist functions from the factoextra package, while the fviz_cluster function was used for cluster scatterplots. Heatmaps were generated to visualize differentially expressed genes using R script.

Statistical analysis and visualization of gene functional profiles and clusters for Gene Ontology terms were carried out using the DOSE and clusterProfiler packages. Ingenuity Pathway Analysis was employed for upstream pathway analysis and identifying pathway activity patterns.

ACKNOWLEDGMENTS

We want to thank all members of the Yoshida laboratory for their constructive feedback on this study. This work was supported by a grant from the Leducq Foundation (18CVD05) and JSPS KAKENHI grants (22K16137 [A.L.-C.], 24K11267 [A.L.-C.], and 21H02912 [Y.Y.]). Research Center Network also provides funding for Realization of Regenerative Medicine, Japan Agency for Medical Research and Development (AMED) (JP19bm0104001 and JP20bm0804022) (Y.Y.), Acceleration Program of R&D and implementation for Regenerative Medicine and Cell and Gene Therapy, AMED (JP23bm1423011 and JP23bm132300) (Y.Y.), the Research on Regulatory Science of Pharmaceuticals and Medical Devices, AMED (JP22mk0101189 and JP22mk0101241) (Y.Y.), the Translational Research grant, AMED (JP22ym0126091) (Y.Y.), and the iPS Cell Research Fund (A.L.-C and Y.Y.). We want to express our gratitude to Rumi Fujihara, Tomomi Gibson, and Hiroko Sata for their administrative support.

AUTHOR CONTRIBUTIONS

A.L.-C. and Y.Y. conceived the study and designed the project. Y. Miyoshi, Y.T., Y. Matsumura, K.T., M. Nishikawa, and A.L.-C. performed the experiments. M. Narita assisted in RNA sequencing. Y. Miyoshi and A.L.-C. analyzed and interpreted the data. Y.Y. and A.L.-C. provided funding and supervision. A.L.-C., Y. Miyoshi, and Y.Y. wrote the manuscript. All authors discussed the results.

DECLARATION OF INTERESTS

Y.Y. is a scientific advisor of Orizuru Therapeutics and receives grants from Takeda Pharmaceutical Company and Altos Labs, Inc. outside the submitted work.

SUPPLEMENTAL INFORMATION

Supplemental information can be found online at https://doi.org/10.1016/j.stemcr.2024.08.008.

Received: March 26, 2024
Revised: August 23, 2024
Accepted: August 26, 2024
Published: September 26, 2024

REFERENCES

Alex, L., Tuleta, I., Harikrishnan, V., and Frangogiannis, N.G. (2022). Validation of Specific and Reliable Genetic Tools to Identify, Label, and Target Cardiac Pericytes in Mice. J. Am. Heart Assoc. *11*, e023171. https://doi.org/10.1161/JAHA.121.023171.

Alex, L., Tuleta, I., Hernandez, S.C., Hanna, A., Venugopal, H., Astorkia, M., Humeres, C., Kubota, A., Su, K., Zheng, D., and

Frangogiannis, N.G. (2023). Cardiac Pericytes Acquire a Fibrogenic Phenotype and Contribute to Vascular Maturation After Myocardial Infarction. Circulation *148*, 882–898. https://doi.org/10.1161/CIRCULATIONAHA.123.064155.

Avolio, E., Campagnolo, P., Katare, R., and Madeddu, P. (2024). The role of cardiac pericytes in health and disease: therapeutic targets for myocardial infarction. Nat. Rev. Cardiol. *21*, 106–118. https://doi.org/10.1038/s41569-023-00913-y.

Bao, X., Lian, X., Hacker, T.A., Schmuck, E.G., Qian, T., Bhute, V.J., Han, T., Shi, M., Drowley, L., Plowright, A., et al. (2016). Long-term self-renewing human epicardial cells generated from pluripotent stem cells under defined xeno-free conditions. Nat. Biomed. Eng. *1*, 0003. https://doi.org/10.1038/s41551-016-0003.

Bergers, G., and Song, S. (2005). The role of pericytes in blood-vessel formation and maintenance. Neuro Oncol. *7*, 452–464. https://doi.org/10.1215/S1152851705000232.

Bouacida, A., Rosset, P., Trichet, V., Guilloton, F., Espagnolle, N., Cordonier, T., Heymann, D., Layrolle, P., Sensébé, L., and Deschaseaux, F. (2012). Pericyte-like progenitors show high immaturity and engraftment potential as compared with mesenchymal stem cells. PLoS One *7*, e48648. https://doi.org/10.1371/journal.pone.0048648.

Carvajal, G., Rodríguez-Vita, J., Rodrigues-Díez, R., Sánchez-López, E., Rupérez, M., Cartier, C., Esteban, V., Ortiz, A., Egido, J., Mezzano, S.A., and Ruiz-Ortega, M. (2008). Angiotensin II activates the Smad pathway during epithelial mesenchymal transdifferentiation. Kidney Int. *74*, 585–595. https://doi.org/10.1038/ki.2008.213.

Chen, D., Xia, Y., Zuo, K., Wang, Y., Zhang, S., Kuang, D., Duan, Y., Zhao, X., and Wang, G. (2015). Crosstalk between SDF-1/CXCR4 and SDF-1/CXCR7 in cardiac stem cell migration. Sci. Rep. *5*, 16813. https://doi.org/10.1038/srep16813.

Chung, H.-J., Kim, J.-T., Kim, H.-J., Kyung, H.-W., Katila, P., Lee, J.-H., Yang, T.-H., Yang, Y.-I., and Lee, S.-J. (2015). Epicardial delivery of VEGF and cardiac stem cells guided by 3-dimensional PLLA mat enhancing cardiac regeneration and angiogenesis in acute myocardial infarction. J. Control. Release *205*, 218–230. https://doi.org/10.1016/j.jconrel.2015.02.013.

Cobb, M.S., Tao, S., Shortt, K., Girgis, M., Hauptman, J., Schriewer, J., Chin, Z., Dorfman, E., Campbell, K., Heruth, D.P., et al. (2022). Smad3 promotes adverse cardiovascular remodeling and dysfunction in doxorubicin-treated hearts. Am. J. Physiol. Heart Circ. Physiol. *323*, H1091–H1107. https://doi.org/10.1152/ajpheart.00312.2022.

Dennler, S., Itoh, S., Vivien, D., ten Dijke, P., Huet, S., and Gauthier, J.-M. (1998). Direct binding of Smad3 and Smad4 to critical TGFβ-inducible elements in the promoter of human plasminogen activator inhibitor-type 1 gene. EMBO J. *17*, 3091–3100. https://doi.org/10.1093/emboj/17.11.3091.

Derynck, R., and Zhang, Y.E. (2003). Smad-dependent and Smad-independent pathways in TGF-beta family signalling. Nature *425*, 577–584. https://doi.org/10.1038/nature02006.

Du, J., Yuan, X., Deng, H., Huang, R., Liu, B., Xiong, T., Long, X., Zhang, L., Li, Y., and She, Q. (2023). Single-cell and spatial heterogeneity landscapes of mature epicardial cells. J. Pharm. Anal. *13*, 894–907. https://doi.org/10.1016/j.jpha.2023.07.011.

Eschenhagen, T., Bolli, R., Braun, T., Field, L.J., Fleischmann, B.K., Frisén, J., Giacca, M., Hare, J.M., Houser, S., Lee, R.T., et al. (2017). Cardiomyocyte Regeneration: A Consensus Statement. Circulation *136*, 680–686. https://doi.org/10.1161/CIRCULATIONAHA.117.029343.

Fang, M., Xiang, F.-L., Braitsch, C.M., and Yutzey, K.E. (2016). Epicardium-derived fibroblasts in heart development and disease. J. Mol. Cell. Cardiol. *91*, 23–27. https://doi.org/10.1016/j.yjmcc.2015.12.019.

Feinberg, M.W., Shimizu, K., Lebedeva, M., Haspel, R., Takayama, K., Chen, Z., Frederick, J.P., Wang, X.-F., Simon, D.I., Libby, P., et al. (2004). Essential Role for Smad3 in Regulating MCP-1 Expression and Vascular Inflammation. Circ. Res. *94*, 601–608. https://doi.org/10.1161/01.RES.0000119170.70818.4F.

Geevarghese, A., and Herman, I.M. (2014). Pericyte-Endothelial Cross-Talk: Implications and Opportunities for Advanced Cellular Therapies. Transl. Res. *163*, 296–306. https://doi.org/10.1016/j.trsl.2014.01.011.

Gittenberger-de Groot, A.C., Winter, E.M., and Poelmann, R.E. (2010). Epicardium-derived cells (EPDCs) in development, cardiac disease and repair of ischemia. J. Cell Mol. Med. *14*, 1056–1060. https://doi.org/10.1111/j.1582-4934.2010.01077.x.

Goumans, M.J., Valdimarsdottir, G., Itoh, S., Lebrin, F., Larsson, J., Mummery, C., Karlsson, S., and ten Dijke, P. (2003). Activin receptor-like kinase (ALK)1 is an antagonistic mediator of lateral TGFbeta/ALK5 signaling. Mol. Cell. *12*, 817–828. https://doi.org/10.1016/s1097-2765(03)00386-1.

Heldin, C.-H., and Moustakas, A. (2016). Signaling Receptors for TGF-β Family Members. Cold Spring Harb. Perspect. Biol. *8*, a022053. https://doi.org/10.1101/cshperspect.a022053.

Hooglugt, A., van der Stoel, M.M., Boon, R.A., and Huveneers, S. (2020). Endothelial YAP/TAZ Signaling in Angiogenesis and Tumor Vasculature. Front. Oncol. *10*, 612802. https://doi.org/10.3389/fonc.2020.612802.

Iyer, D., Gambardella, L., Bernard, W.G., Serrano, F., Mascetti, V.L., Pedersen, R.A., Talasila, A., and Sinha, S. (2015). Robust derivation of epicardium and its differentiated smooth muscle cell progeny from human pluripotent stem cells. Development *142*, 1528–1541. https://doi.org/10.1242/dev.119271.

Jackman, C.P., Ganapathi, A.M., Asfour, H., Qian, Y., Allen, B.W., Li, Y., and Bursac, N. (2018). Engineered cardiac tissue patch maintains structural and electrical properties after epicardial implantation. Biomaterials *159*, 48–58. https://doi.org/10.1016/j.biomaterials.2018.01.002.

Junghof, J., Kogure, Y., Yu, T., Verdugo-Sivianes, E.M., Narita, M., Lucena-Cacace, A., and Yoshida, Y. (2022). CDH18 is a fetal epicardial biomarker regulating differentiation towards vascular smooth muscle cells. NPJ Regen. Med. *7*, 14. https://doi.org/10.1038/s41536-022-00207-w.

Kang, Y., and Massagué, J. (2004). Epithelial-Mesenchymal Transitions: Twist in Development and Metastasis. Cell *118*, 277–279. https://doi.org/10.1016/j.cell.2004.07.011.

Kasamoto, M., Funakoshi, S., Hatani, T., Okubo, C., Nishi, Y., Tsujisaka, Y., Nishikawa, M., Narita, M., Ohta, A., Kimura, T., and Yoshida, Y. (2023). Am80, a retinoic acid receptor agonist, activates the cardiomyocyte cell cycle and enhances engraftment in the heart. Stem Cell Rep. *18*, 1672–1685. https://doi.org/10.1016/j.stemcr.2023.06.006.

Knight-Schrijver, V.R., Davaapil, H., Bayraktar, S., Ross, A.D.B., Kanemaru, K., Cranley, J., Dabrowska, M., Patel, M., Polanski, K., He, X., et al. (2022). A single-cell comparison of adult and fetal human epicardium defines the age-associated changes in epicardial activity. Nat. Cardiovasc. Res. *1*, 1215–1229. https://doi.org/10.1038/s44161-022-00183-w.

Kobayashi, K., Maeda, K., Takefuji, M., Kikuchi, R., Morishita, Y., Hirashima, M., and Murohara, T. (2017). Dynamics of angiogenesis in ischemic areas of the infarcted heart. Sci. Rep. *7*, 7156. https://doi.org/10.1038/s41598-017-07524-x.

Lerman, D.A., Diaz, M., and Peault, B. (2018). Changes in coexpression of pericytes and endogenous cardiac progenitor cells from heart development to disease state. Eur. Heart J. *39*, P1850. https://doi.org/10.1093/eurheartj/ehy565.P1850.

Li, B., Wang, Z., Yang, F., Huang, J., Hu, X., Deng, S., Tian, M., and Si, X. (2021). miR-449a-5p suppresses CDK6 expression to inhibit cardiomyocyte proliferation. Mol. Med. Rep. *23*, 14. https://doi.org/10.3892/mmr.2020.11652.

Li, J., Zhao, Y., and Zhu, W. (2022). Targeting angiogenesis in myocardial infarction: Novel therapeutics (Review). Exp. Ther. Med. *23*, 64. https://doi.org/10.3892/etm.2021.10986.

Lim, G.B. (2021). Heterogeneity of the post-infarct epicardium. Nat. Rev. Cardiol. *18*, 612. https://doi.org/10.1038/s41569-021-00596-3.

Lin, Z., and Pu, W.T. (2014). Strategies for cardiac regeneration and repair. Sci. Transl. Med. *6*, 239rv1. https://doi.org/10.1126/scitranslmed.3006681.

Loh, C.-Y., Chai, J.Y., Tang, T.F., Wong, W.F., Sethi, G., Shanmugam, M.K., Chong, P.P., and Looi, C.Y. (2019). The E-Cadherin and N-Cadherin Switch in Epithelial-to-Mesenchymal Transition: Signaling, Therapeutic Implications, and Challenges. Cells *8*, 1118. https://doi.org/10.3390/cells8101118.

Massagué, J., Seoane, J., and Wotton, D. (2005). Smad transcription factors. Genes Dev. *19*, 2783–2810. https://doi.org/10.1101/gad.1350705.

Murganti, F., Derks, W., Baniol, M., Simonova, I., Trus, P., Neumann, K., Khattak, S., Guan, K., and Bergmann, O. (2022). FUCCI-Based Live Imaging Platform Reveals Cell Cycle Dynamics and Identifies Pro-proliferative Compounds in Human iPSC-Derived Cardiomyocytes. Front. Cardiovasc. Med. *9*, 840147.

Nakagawa, T., Li, J.H., Garcia, G., Mu, W., Piek, E., Böttinger, E.P., Chen, Y., Zhu, H.J., Kang, D.-H., Schreiner, G.F., et al. (2004). TGF-β induces proangiogenic and antiangiogenic factorsvia parallel but distinct Smad pathways1. Kidney Int. *66*, 605–613. https://doi.org/10.1111/j.1523-1755.2004.00780.x.

Olivey, H.E., and Svensson, E.C. (2010). Epicardial-Myocardial Signaling Directing Coronary Vasculogenesis. Circ. Res. *106*, 818–832. https://doi.org/10.1161/CIRCRESAHA.109.209197.

Quijada, P., Trembley, M.A., Misra, A., Myers, J.A., Baker, C.D., Pérez-Hernández, M., Myers, J.R., Dirkx, R.A., Cohen, E.D., Delmar, M., et al. (2021). Coordination of endothelial cell positioning and fate specification by the epicardium. Nat. Commun. *12*, 4155. https://doi.org/10.1038/s41467-021-24414-z.

Quijada, P., Park, S., Zhao, P., Kolluri, K.S., Wong, D., Shih, K.D., Fang, K., Pezhouman, A., Wang, L., Daraei, A., et al. (2023). Cardiac pericytes mediate the remodeling response to myocardial infarction. J. Clin. Invest. *133*, e162188. https://doi.org/10.1172/JCI162188.

Renko, O., Tolonen, A.-M., Rysä, J., Magga, J., Mustonen, E., Ruskoaho, H., and Serpi, R. (2018). SDF1 gradient associates with the distribution of c-Kit+ cardiac cells in the heart. Sci. Rep. *8*, 1160. https://doi.org/10.1038/s41598-018-19417-8.

Rhee, J.-W., and Wu, J.C. (2018). Cardiac Cell Cycle Activation as a Strategy to Improve iPSC-Derived Cardiomyocyte Therapy. Circ. Res. *122*, 14–16. https://doi.org/10.1161/CIRCRESAHA.117.312287.

Roman, B.L., and Hinck, A.P. (2017). ALK1 signaling in development and disease: new paradigms. Cell. Mol. Life Sci. *74*, 4539–4560. https://doi.org/10.1007/s00018-017-2636-4.

Rossi, E., Bernabeu, C., and Smadja, D.M. (2019). Endoglin as an Adhesion Molecule in Mature and Progenitor Endothelial Cells: A Function Beyond TGF-β. Front. Med. *6*, 10.

Shen, M., Liu, C., Zhao, S.R., Manhas, A., Sundaram, L., Ameen, M., and Wu, J.C. (2023). Stepwise Generation of Human Induced Pluripotent Stem Cell-Derived Cardiac Pericytes to Model Coronary Microvascular Dysfunction. Circulation *147*, 515–518. https://doi.org/10.1161/CIRCULATIONAHA.122.061770.

Smits, A.M., Dronkers, E., and Goumans, M.-J. (2018). The epicardium as a source of multipotent adult cardiac progenitor cells: Their origin, role and fate. Pharmacol. Res. *127*, 129–140. https://doi.org/10.1016/j.phrs.2017.07.020.

Smyth, L.C.D., Highet, B., Jansson, D., Wu, J., Rustenhoven, J., Aalderink, M., Tan, A., Li, S., Johnson, R., Coppieters, N., et al. (2022). Characterisation of PDGF-BB:PDGFRβ signalling pathways in human brain pericytes: evidence of disruption in Alzheimer's disease. Commun. Biol. *5*, 235. https://doi.org/10.1038/s42003-022-03180-8.

Sridurongrit, S., Larsson, J., Schwartz, R., Ruiz-Lozano, P., and Kaartinen, V. (2008). Signaling via the Tgf-β type I receptor Alk5 in heart development. Dev. Biol. *322*, 208–218. https://doi.org/10.1016/j.ydbio.2008.07.038.

Streef, T.J., and Smits, A.M. (2021). Epicardial Contribution to the Developing and Injured Heart: Exploring the Cellular Composition of the Epicardium. Front. Cardiovasc. Med. *8*, 750243.

Suffee, N., Moore-Morris, T., Jagla, B., Mougenot, N., Dilanian, G., Berthet, M., Proukhnitzky, J., Le Prince, P., Tregouet, D.A., Pucéat, M., and Hatem, S.N. (2020). Reactivation of the Epicardium at the Origin of Myocardial Fibro-Fatty Infiltration During the Atrial Cardiomyopathy. Circ. Res. *126*, 1330–1342. https://doi.org/10.1161/CIRCRESAHA.119.316251.

Takahashi, K., and Yamanaka, S. (2006). Induction of pluripotent stem cells from mouse embryonic and adult fibroblast cultures

by defined factors. Cell *126*, 663–676. https://doi.org/10.1016/j.cell.2006.07.024.

Takahashi, K., Tanabe, K., Ohnuki, M., Narita, M., Ichisaka, T., Tomoda, K., and Yamanaka, S. (2007). Induction of pluripotent stem cells from adult human fibroblasts by defined factors. Cell *131*, 861–872. https://doi.org/10.1016/j.cell.2007.11.019.

Tan, J.J., Guyette, J.P., Miki, K., Xiao, L., Kaur, G., Wu, T., Zhu, L., Hansen, K.J., Ling, K.-H., Milan, D.J., and Ott, H.C. (2021). Human iPS-derived pre-epicardial cells direct cardiomyocyte aggregation expansion and organization in vitro. Nat. Commun. *12*, 4997. https://doi.org/10.1038/s41467-021-24921-z.

Tao, Z., Chen, B., Tan, X., Zhao, Y., Wang, L., Zhu, T., Cao, K., Yang, Z., Kan, Y.W., and Su, H. (2011). Coexpression of VEGF and angiopoietin-1 promotes angiogenesis and cardiomyocyte proliferation reduces apoptosis in porcine myocardial infarction (MI) heart. Proc. Natl. Acad. Sci. USA *108*, 2064–2069. https://doi.org/10.1073/pnas.1018925108.

Tzavlaki, K., and Moustakas, A. (2020). TGF-β Signaling. Biomolecules *10*, 487. https://doi.org/10.3390/biom10030487.

Volz, K.S., Jacobs, A.H., Chen, H.I., Poduri, A., McKay, A.S., Riordan, D.P., Kofler, N., Kitajewski, J., Weissman, I., and Red-Horse, K. (2015). Pericytes are progenitors for coronary artery smooth muscle. Elife *4*, e10036. https://doi.org/10.7554/eLife.10036.

Whitehead, A.J., Hocker, J.D., Ren, B., and Engler, A.J. (2022). Improved epicardial cardiac fibroblast generation from iPSCs. J. Mol. Cell. Cardiol. *164*, 58–68. https://doi.org/10.1016/j.yjmcc.2021.11.011.

van Wijk, B., Gunst, Q.D., Moorman, A.F.M., and van den Hoff, M.J.B. (2012). Cardiac regeneration from activated epicardium. PLoS One *7*, e44692. https://doi.org/10.1371/journal.pone.0044692.

Witty, A.D., Mihic, A., Tam, R.Y., Fisher, S.A., Mikryukov, A., Shoichet, M.S., Li, R.-K., Kattman, S.J., and Keller, G. (2014). Generation of the epicardial lineage from human pluripotent stem cells. Nat. Biotechnol. *32*, 1026–1035. https://doi.org/10.1038/nbt.3002.

Yamazaki, T., and Mukouyama, Y.S. (2018). Tissue Specific Origin, Development, and Pathological Perspectives of Pericytes. Front. Cardiovasc. Med. *5*, 78.

Yin, H., Li, X., Hu, S., Liu, T., Yuan, B., Gu, H., Ni, Q., Zhang, X., and Zheng, F. (2013). IL-33 accelerates cutaneous wound healing involved in upregulation of alternatively activated macrophages. Mol. Immunol. *56*, 347–353. https://doi.org/10.1016/j.molimm.2013.05.225.

Yuan, K., Orcholski, M.E., Huang, N.F., and de Jesus Perez, V.A. (2016). In Vivo Study of Human Endothelial-Pericyte Interaction Using the Matrix Gel Plug Assay in Mouse. J. Vis. Exp. *54617*, 54617. https://doi.org/10.3791/54617.

Zabini, D., Granton, E., Hu, Y., Miranda, M.Z., Weichelt, U., Breuils Bonnet, S., Bonnet, S., Morrell, N.W., Connelly, K.A., Provencher, S., et al. (2018). Loss of SMAD3 Promotes Vascular Remodeling in Pulmonary Arterial Hypertension via MRTF Disinhibition. Am. J. Respir. Crit. Care Med. *197*, 244–260. https://doi.org/10.1164/rccm.201702-0386OC.

Zhang, Q., Chen, L., Huang, L., Cheng, H., Wang, L., Xu, L., Hu, D., He, C., Fu, C., and Wei, Q. (2022). CD44 promotes angiogenesis in myocardial infarction through regulating plasma exosome uptake and further enhancing FGFR2 signaling transduction. Mol. Med. *28*, 145. https://doi.org/10.1186/s10020-022-00575-5.

Zhu, S., Chen, M., Ying, Y., Wu, Q., Huang, Z., Ni, W., Wang, X., Xu, H., Bennett, S., Xiao, J., and Xu, J. (2022). Versatile subtypes of pericytes and their roles in spinal cord injury repair, bone development and repair. Bone Res. *10*, 30. https://doi.org/10.1038/s41413-022-00203-2.

Stem Cell Reports, Volume *19*

Supplemental Information

SMAD3 mediates the specification of human induced pluripotent stem cell-derived epicardium into progenitors for the cardiac pericyte lineage

Yutaro Miyoshi, Antonio Lucena-Cacace, Yu Tian, Yasuko Matsumura, Kanae Tani, Misato Nishikawa, Megumi Narita, Takeshi Kimura, Koh Ono, and Yoshinori Yoshida

SUPPLEMENTAL INFORMATION

Figure S1

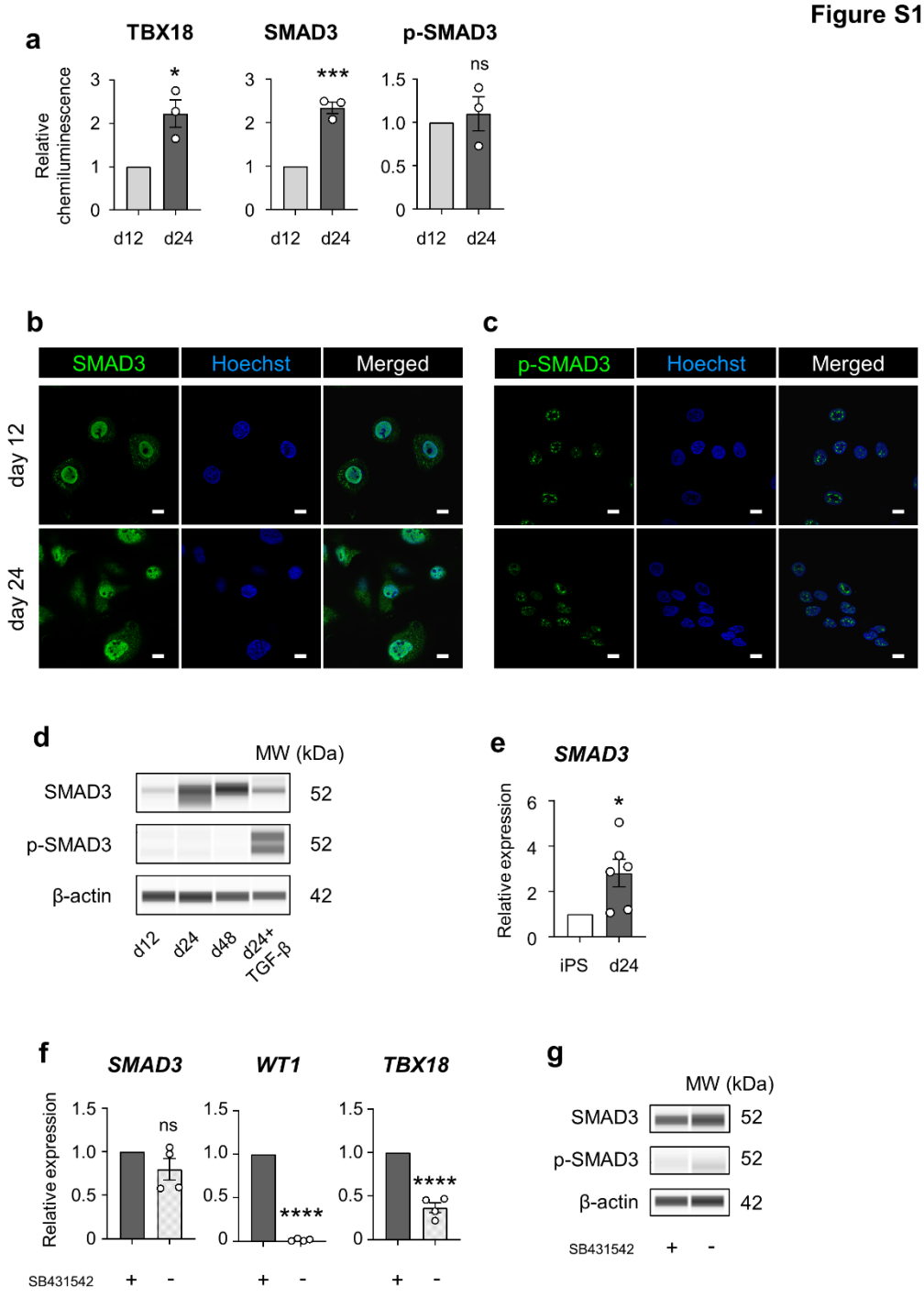

Figure S2

Figure S2

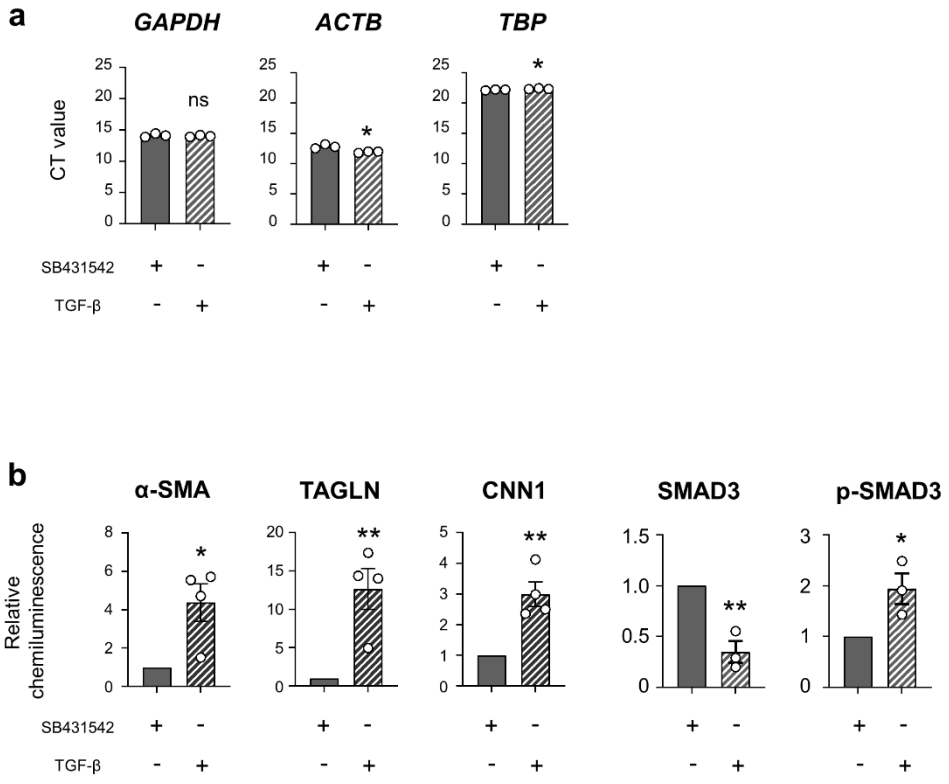

Figure S3

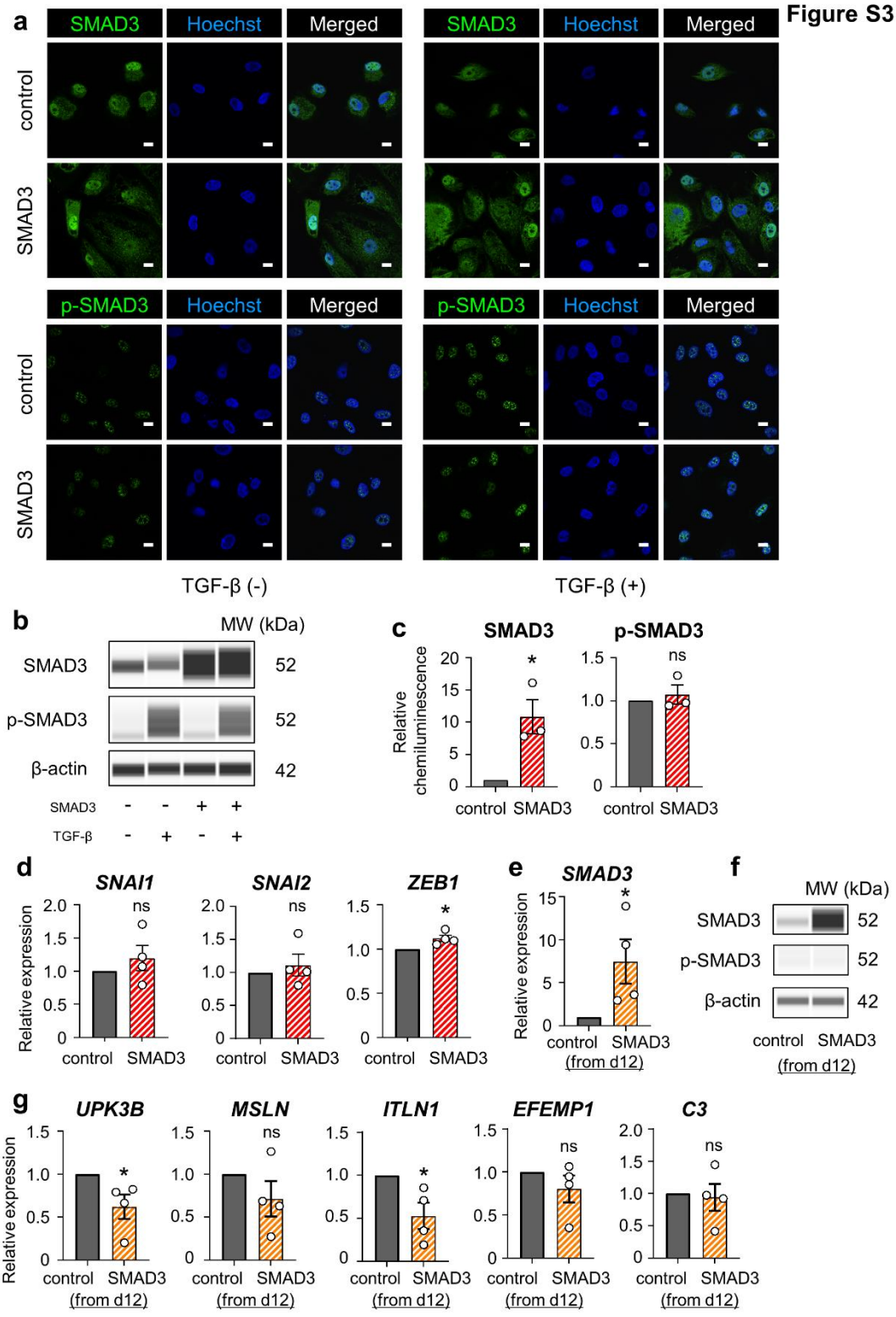
Figure S3
a
SMAD3
Hoechst
Merged
control
SMAD3
p-SMAD3
TGF-β (-)
TGF-β (+)
b
MW (kDa)
SMAD3
p-SMAD3
β-actin
52
42
TGF-β
c
SMAD3
p-SMAD3
Relative chemiluminescence
ns
control
d
SNAI1
SNAI2
ZEB1
Relative expression
e
SMAD3
(from d12)
f
g
UPK3B
MSLN
ITLN1
EFEMP1
C3

Figure S4

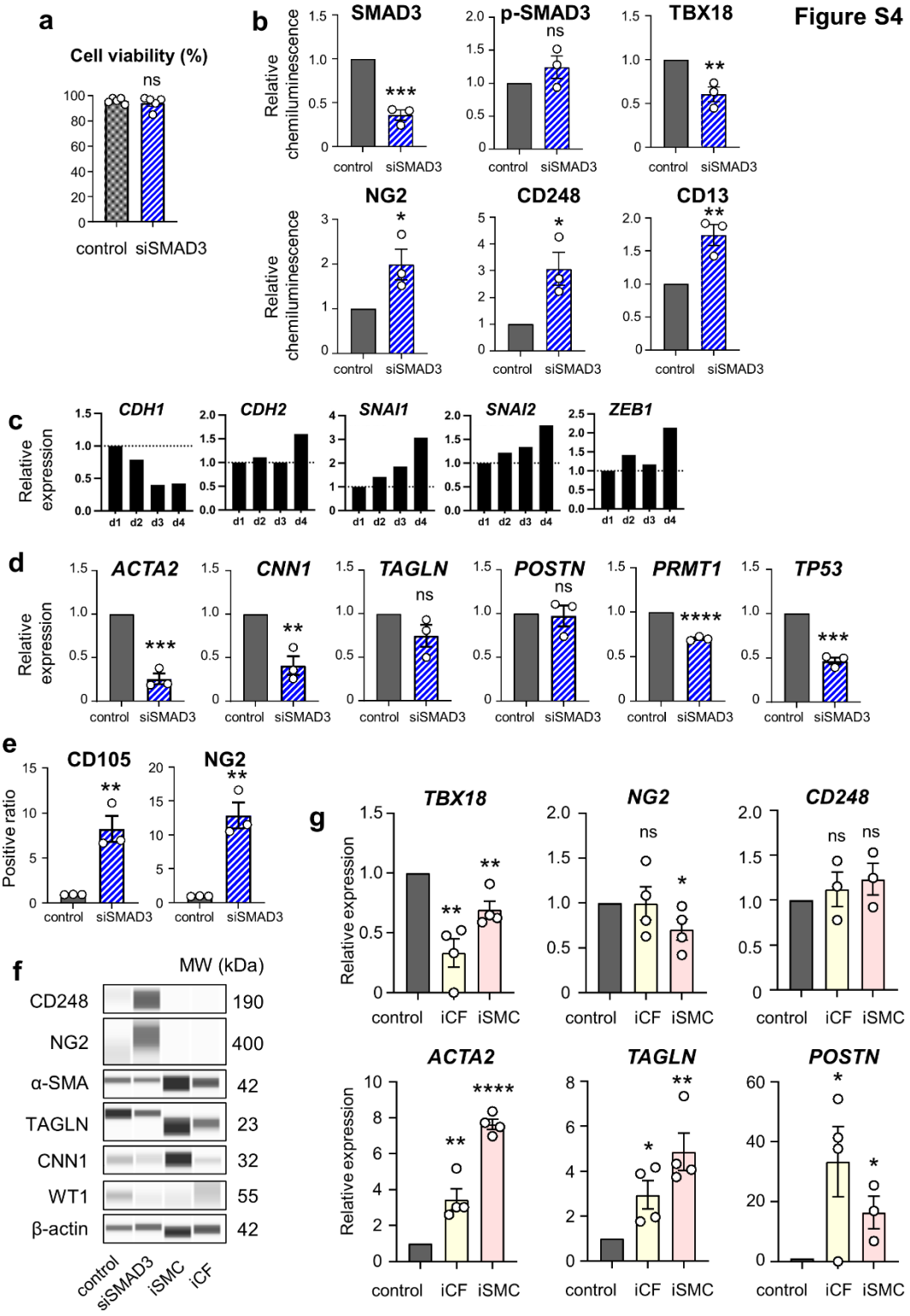
Figure S4
a
Cell viability (%)
ns
control siSMAD3
b
SMAD3
p-SMAD3
TBX18
NG2
CD248
CD13
Relative chemiluminescence
control siSMAD3
c
CDH1
CDH2
SNAI1
SNAI2
ZEB1
Relative expression
d1 d2 d3 d4
d
ACTA2
CNN1
TAGLN
POSTN
PRMT1
TP53
Relative expression
e
CD105
NG2
Positive ratio
f
MW (kDa)
CD248 190
NG2 400
α-SMA 42
TAGLN 23
CNN1 32
WT1 55
β-actin 42
control siSMAD3 iSMC iCF
g
TBX18
NG2
CD248
ACTA2
TAGLN
POSTN
Relative expression
control iCF iSMC

Figure S5

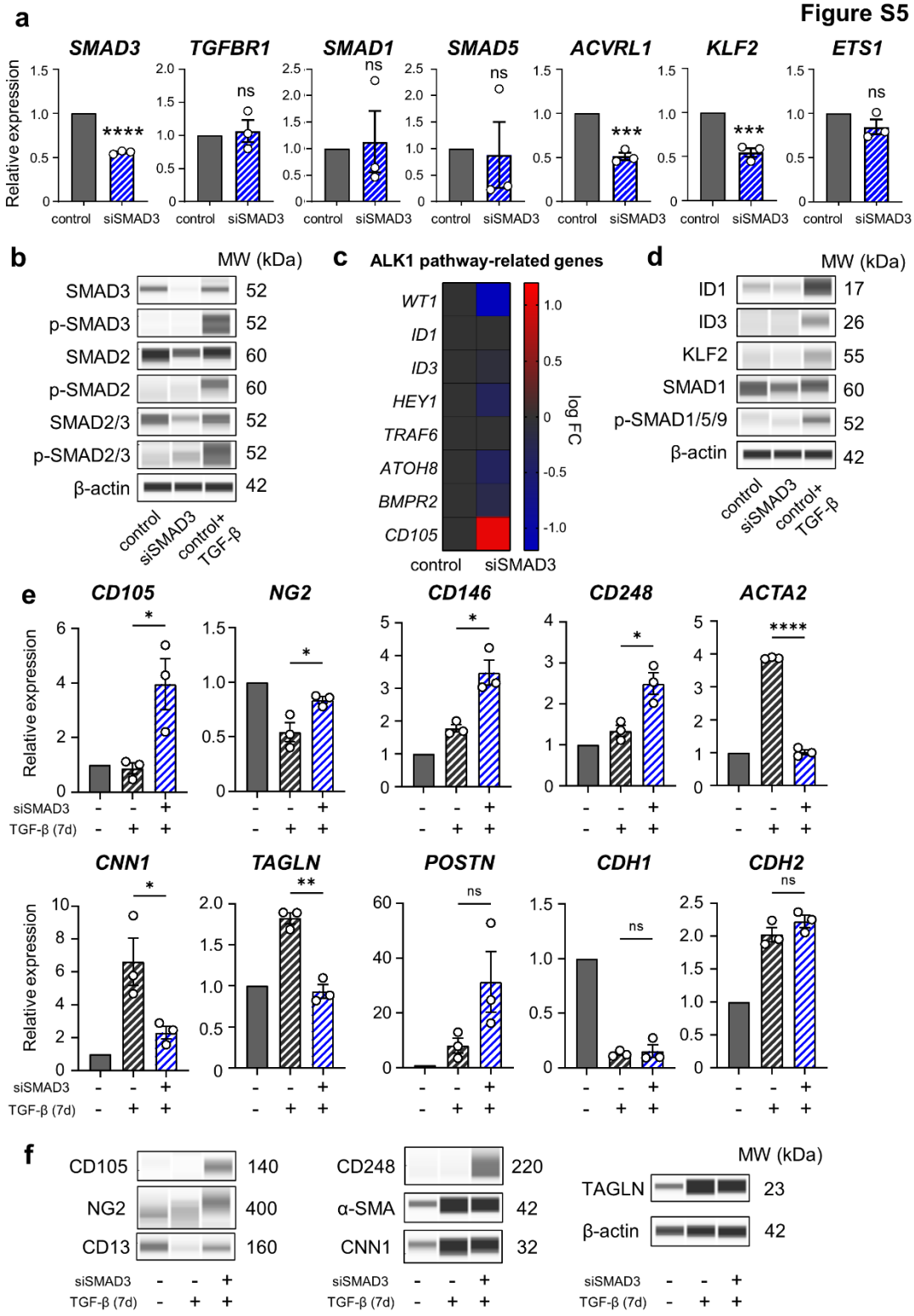
Figure S5
a
SMAD3
TGFBR1
SMAD1
SMAD5
ACVRL1
KLF2
ETS1
Relative expression
control
siSMAD3
b
MW (kDa)
SMAD3
p-SMAD3
SMAD2
p-SMAD2
SMAD2/3
p-SMAD2/3
β-actin
control
siSMAD3
control+ TGF-β
c
ALK1 pathway-related genes
WT1
ID1
ID3
HEY1
TRAF6
ATOH8
BMPR2
CD105
log FC
d
ID1
ID3
KLF2
SMAD1
p-SMAD1/5/9
β-actin
e
CD105
NG2
CD146
CD248
ACTA2
CNN1
TAGLN
POSTN
CDH1
CDH2
siSMAD3
TGF-β (7d)
f
CD105
NG2
CD13
CD248
α-SMA
CNN1
TAGLN
β-actin

Figure S6

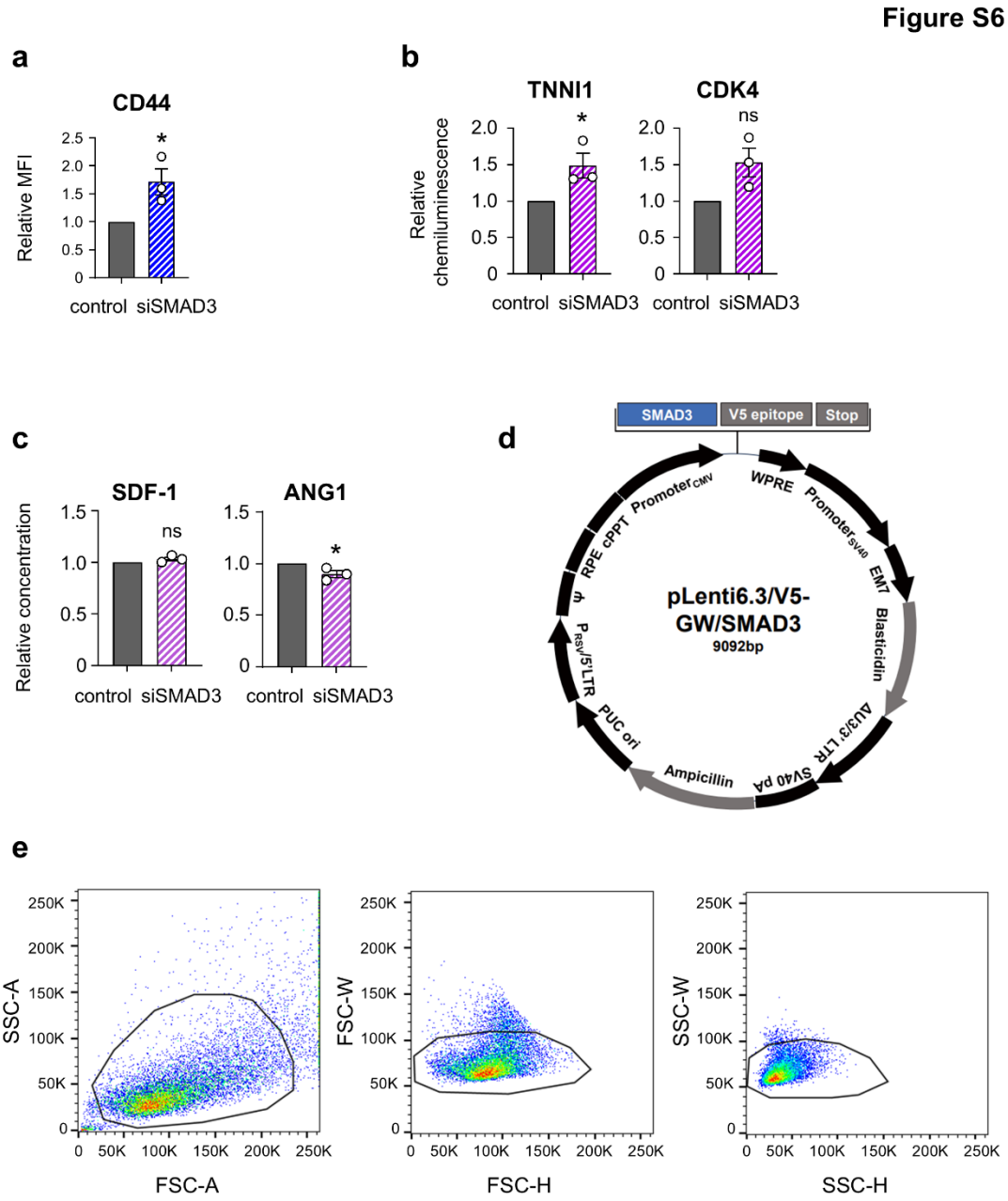
Figure S6
a
CD44
Relative MFI
control siSMAD3
b
TNNI1
CDK4
ns
Relative chemiluminescence
control siSMAD3 control siSMAD3
c
SDF-1
ANG1
ns
Relative concentration
control siSMAD3 control siSMAD3
d
SMAD3
V5 epitope
Stop
pLenti6.3/V5-GW/SMAD3
9092bp
Promoter CMV
WPRE
Promoter SV40
EM7
Blasticidin
ΔU3/3' LTR
SV40 pA
Ampicillin
PUC ori
P RSV/5' LTR
Ψ
RPE cPPT
e
SSC-A
FSC-A
FSC-W
FSC-H
SSC-W
SSC-H

Figure S1. Detailed SMAD3 dynamics and distribution in epicardial development including the effect of SB431542 (related to Figure 1)

(a). The quantitative analysis of Western blot in Figure 1j (TBX18) and 1l (SMAD3 and p-SMAD3) using relative value of the chemiluminescence [n=3; *p = 0.019, ***p = 0.0006, ns = not significant]. **(b,c).** Immunocytochemistry images for total SMAD3 **(b)** and phosphorylated SMAD3 **(c)** in hiPSC-derived epicardial cell (EPI cells) at day 12 and day 24. **(d).** Time-course analysis for proteins of total and phosphorylated SMAD3 at day 12, day 24, day 48, and a positive control (day 24+TGF-β for 1 hour). **(e).** Quantitative RT-PCR (qRT-PCR) analysis of *SMAD3* in hiPSCs and EPI cells at day 24 [n=6; *p = 0.015]. **(f).** qRT-PCR analysis of *SMAD3* and epicardial markers (*WT1* and *TBX18*) in control EPI cells (SB431542+) and EPI cells without SB431542 for 7 days [n=4, ****p < 0.0001, ns = not significant]. **(g).** Western blot analysis of total and phosphorylated SMAD3 in control EPI cells (SB431542+) and EPI cells without SB431542 for 7 days. [All error bars represent standard error of the mean (SEM); the graph plots are derived from experimental replicates, obtained from independent batches; statistical analysis was performed using a two-sided unpaired Student's t-test; scale bars equal 10 μm.]

Figure S2. Information of housekeeping genes and quantification of protein analysis in the context of EMT (related to Figure 2)

(a). CT values in quantitative RT-PCR (qRT-PCR) analysis of housekeeping genes (*GAPDH, ACTB,* and *TBP)* in hiPSC-derived epicardial cells (EPI cells) treated with TGF-β and SB431542 for three days, post day 24 [*p < 0.05, ns = not significant]. **(b).** The quantitative analysis of Western blot in Figure 2f (α-SMA, TAGLN, and CNN1) and 2h (SMAD3 and p-SMAD3) using relative value of the chemiluminescence [n=3 or 4; *p < 0.05, **p < 0.01]. [All error bars represent standard error of the mean (SEM); the graph plots are derived from experimental replicates, obtained from independent batches; statistical analysis was performed using a two-sided unpaired Student's t-test.]

Figure S3. Comparison of endogenous and overexpressed SMAD3 under TGF-β stimulation and overexpression at more immature stage (related to Figure 3)

(a). Immunocytochemistry images for total and phosphorylated SMAD3 in control and SMAD3-overexpressing hiPSC-derived epicardial cell (EPI cells) with or without TGF-β for 1 hour. **(b).** Western blot analysis of total and phosphorylated SMAD3 in control and SMAD3-overexpressing EPI cells with or without TGF-β for 1 hour. **(c).** The quantitative analysis of Western blot in Figure 3d (SMAD3 and p-SMAD3) using relative value of the chemiluminescence [n=3; *p = 0.020, ns = not significant]. **(d).** Quantitative RT-PCR (qRT-PCR) analysis for *SNAI1, SNAI2,* and *ZEB1* [n=4; *p = 0.015]. **(e,f).** Validation of SMAD3 overexpression in qRT-PCR **(e)** and Western blot **(f)** in EPI cells overexpressed SMAD3 from day 12 [n=3; *p = 0.022]. **(g).** qRT-PCR for mature epicardial markers: *UPK3B, MSLN, ITLN1, EFEMP1,* and *C3* [n=4: *p < 0.05, ns = not significant]. [All error bars represent standard error of the mean (SEM); the graph plots are derived from experimental replicates, obtained from independent batches; statistical analysis was performed using a two-sided unpaired Student's t-test; scale bars equal 10 μm.]

Figure S4. Characterization of specific EMT towards cardiac pericyte progenitors induced by SMAD3 silencing (related to Figure 4)

(a). Cell viability of SMAD3-silenced and control hiPSC-derived epicardial cell (EPI cells) 7 days after siRNA transfection [n=5; ns = not significant]. **(b).** The quantitative analysis of Western blot in Figure 4d (SMAD3 and p-SMAD3), 4h (TBX18), and 4i (NG2, CD248, and CD13) using relative value of the chemiluminescence [n=3; *p < 0.05, **p < 0.01, ***p = 0.0004]. **(c).** Time-course (days) of the mRNA expression analysis (RNA-Seq derived) for *CDH1, CDH2, SNAI1, SNAI2* and *ZEB1* during SMAD3 downregulation in EPI cells. Values are expressed as a ratio to day 1. **(d).** Quantitative RT-PCR (qRT-PCR) analysis of SMAD3-silenced EPI cells (siSMAD3) compared to control for the EPDC markers (*ACTA2, CNN1, TAGLN* and *POSTN*) and *PRMT1* and *TP53* [n=3; ** p < 0.01, ***p < 0.001, ****p < 0.0001, ns = not significant]. **(e).** The quantitative analysis of flow cytometry in Figure 4l-o, indicating the

percentage of positive population for CD105 and NG2 [n=3, **p < 0.01]. **(f).** Protein expression analysis for cardiac pericytes, EPDCs and epicardial markers (cardiac pericytes- NG2, CD248; EPDCs- α-SMA, TAGLN, and CNN1; epicardial- WT1) in control and siSMAD3-EPI cells compared to induced cardiac fibroblasts (iCF) and induced smooth muscle cells (iSMC). **(g).** qRT-PCR analysis for epicardial, cardiac pericytes and EPDCs markers (epicardial- *TBX18*; cardiac pericytes- *NG2, CD248*; EPDCs- *ACTA2, TAGLN,* and *POSTN*) in iCF and iSMC compared to control EPI cells maintained in SB431542 [n=3 or 4; *p < 0.05, ** p < 0.01, ****p < 0.0001, ns = not significant].

[All error bars represent standard error of the mean (SEM); the graph plots are derived from experimental replicates, obtained from independent batches; statistical analysis was performed using a two-sided unpaired Student's t-test; scrambled siRNA was used as a control.]

Figure S5. Dynamics of ALK5 and ALK1 pathway-related markers and the independent role of SMAD3 silencing from canonical TGF-β pathway (related to Figure 4)

(a). Quantitative RT-PCR (qRT-PCR) analysis of SMAD3-silenced (siSMAD3) hiPSC-derived epicardial cell (EPI cells) compared to control for ALK5-related genes (*SMAD3* and *TGFBR1*) and ALK1-related genes (*SMAD1, SMAD5, ACVRL1, KLF2* and *ETS1*) [n=3; ***p < 0.001, ****p < 0.0001, ns = not significant]. **(b).** Protein expression analysis for ALK5 pathway-related SMAD families, including positive control (treated by TGF-β for 1 hour). **(c).** RNA-seq-derived heatmap illustrating ALK1 pathway-related genes and transcriptional factors, including WT1 and CD105 as a negative and positive control. **(d).** Protein expression analysis for ALK1 pathway-related SMAD families and the downstream markers with positive control. **(e).** qRT-PCR analysis for cardiac pericyte markers (*CD105, NG2, CD146,* and *CD248*), EPDCs markers (*ACTA2, CNN1, TAGLN,* and *POSTN*), *CDH1* and *CDH2* of TGF-β-treated cells with scrambled siRNA (siSMAD3-) or siSMAD3 (siSMAD3+) compared to control EPI cells. **(f).** Protein expression analysis for cardiac pericyte markers (CD105, NG2, CD13, and CD248)

and EPDCs markers (α-SMA, CNN1, and TAGLN) of TGF-β-treated cells with scrambled siRNA (siSMAD3-) or siSMAD3 (siSMAD3+) compared to control EPI cells.

[All error bars represent standard error of the mean (SEM); the graph plots are derived from experimental replicates, obtained from independent batches; statistical analysis was performed using a two-sided unpaired Student's t-test; scrambled siRNA was used as a control.]

Figure S6. Information of protein analysis quantification and other data in relation to each experiment (related to Figures 5, 6 and experimental procedures)

(a). The quantitative analysis of flow cytometry in Figure 5e, indicating the relative value of mean fluorescence intensity (MFI) for CD44 [n=3, *p = 0.038]. **(b).** The quantitative analysis of Western blot in Figure 6g (TNNI1 and CDK4) using relative value of the chemiluminescence [n=3; *p = 0.047, ns = not significant]. **(c).** ELISA showing that SDF-1 and ANG1 concentration in the supernatant from SMAD3-silenced EPI cells was 73.3 and 154.2 pg/ml, 1.03 and 0.90 times compared to control, respectively [n=3; *p = 0.041, ns = not significant]. **(d).** Schematic representation of pLenti6.3/V5-GW/SMAD3 containing human SMAD3 cDNA under a CMV promoter for gene overexpression. **(e).** Representative FSC/SSC gating and doublet elimination using FSC and SSC.

[All error bars represent standard error of the mean (SEM); the graph plots are derived from experimental replicates, obtained from independent batches; statistical analysis was performed using a two-sided unpaired Student's t-test; scrambled siRNA was used as a control.]

Table S1: List of qRT-PCR primers (related to figures 1, 2, 3, 4, 6, S1, S2, S3, S4, S5)

Genes	**Sequences (5'-3')**
GAPDH	**F:** GGAGCGAGATCCCTCCAAAAT
	R: GGCTGTTGTCATACTTCTCATGG
WT1	**F:** CAGCTTGAATGCATGACCTG
	R: GATGCCGACCGTACAAGAGT
TBX18	**F:** TTAACCTTGTCCGTCTGCCTGAGT
	R: GTAATGGGCTTTGGCCTTTGCACT
SMAD2	**F:** CGTCCATCTTGCCATTCACG
	R: CTCAAGCTCATCTAATCGTCCTG
SMAD3	**F:** TGGACGCAGGTTCTCCAAAC
	R: CCGGCTCGCAGTAGGTAAC
SMAD4	**F:** CTCATGTGATCTATGCCCGTC
	R: AGGTGATACAACTCGTTCGTAGT
CDH1	**F:** CGAGAGCTACACGTTCACGG
	R: GGGTGTCGAGGGAAAAATAGG
CDH2	**F:** CTCCAATCAACTTGCCAGAA
	R: ATACCAGTTGGAGGCTGGTC
ACTA2	**F:** TCAATGTCCCAGCCATGTAT
	R: CAGCACGATGCCAGTTGT
CNN1	**F:** CTGTCAGCCGAGGTTAAGAAC
	R: GAGGCCGTCCATGAAGTTGTT
PDGFRA	**F:** TGGCAGTACCCCATGTCTGAA
	R: CCAAGACCGTCACAAAAAGGC
TAGLN	**F:** AGTGCAGTCCAAAATCGAGAAG
	R: CTTGCTCAGAATCACGCCAT
ALDH1A2	**F:** CTCCTCTGTCACACCCCATT
	R: TTGACAGCTGGAAAGATGGA
BNC1	**F:** CTGTACTCTGAACTGTAGTTGCC
	R: CCATGCTTGCATTGGTCACAC
UPK3B	**F:** TGCCCTACACACCACAGATAA
	R: GCAAGCCCATCGAAGACAC
MSLN	**F:** CCAACCCACCTAACATTTCCAG
	R: CAGCAGGTCCAATGGGAGG
ITLN1	**F:** ACGTGCCCAATAAGTCCCC
	R: CCGTTGTCAGTCCAACACTTTC
EFEMP1	**F:** GTCACAGGACACCGAAGAAAC
	R: TTGCATTGCTGTCTCACAGGA
C3	**F:** GGGGAGTCCCATGTACTCTATC
	R: GGAAGTCGTGGACAGTAACAG
RGS5	**F:** GACATGGCCCAGAAAAGAATCC
	R: CACAAAGCGAGGCAGAGAATC
DLK-1	**F:** CTTTCGGCCACAGCACCTAT
	R: TGTCATCCTCGCAGAATCCAT
ANPEP (CD13)	**F:** GACCAAAGTAAAGCGTGGAATCG
	R: TCTCAGCGTCACCCGGTAG
MCAM (CD146)	**F:** AGCTCCGCGTCTACAAAGC
	R: CTACACAGGTAGCGACCTCC
TEM1 (CD248)	**F:** AGTGTTATTGTAGCGAGGGACA
	R: CCTCTGGGAAGCTCGGTCTA
ENG (CD105)	**F:** TGCACTTGGCCTACAATTCCA
	R: AGCTGCCCACTCAAGGATCT

NG2	**F:** CTTTGACCCTGACTATGTTGGC
	R: TGCAGGCGTCCAGAGTAGA
TNNI1	**F:** CCGGAAGTCGAGAGAAAACCC
	R: TCAATGTCGTATCGCTCCTCA
CDK4	**F:** ATGGCTACCTCTCGATATGAGC
	R: CATTGGGGACTCTCACACTCT
CDK6	**F:** TCTTCATTCACACCGAGTAGTGC
	R: TGAGGTTAGAGCCATCTGGAAA
CCND1	**F:** GCTGCGAAGTGGAAACCATC
	R: CCTCCTTCTGCACACATTTGAA
ACTB	**F:** CATGTACGTTGCTATCCAGGC
	R: CTCCTTAATGTCACGCACGAT
TBP	**F:** CCACTCACAGACTCTCACAAC
	R: CTGCGGTACAATCCCAGAACT
SNAI1	**F:** TCGGAAGCCTAACTACAGCGA
	R: AGATGAGCATTGGCAGCGAG
SNAI2	**F:** CGAACTGGACACACATACAGTG
	R: CTGAGGATCTCTGGTTGTGGT
ZEB1	**F:** GATGATGAATGCGAGTCAGATGC
	R: ACAGCAGTGTCTTGTTGTTGT
TP53	**F:** CAGCACATGACGGAGGTTGT
	R: TCATCCAAATACTCCACACGC
PRMT1	**F:** CTTTGACTCCTACGCACACTT
	R: GTGCCGGTTATGAAACATGGA
TGFBR1	**F:** ACGGCGTTACAGTGTTTCTG
	R: GCACATACAAACGGCCTATCTC
SMAD1	**F:** AGAGACTTCTTGGGTGGAAACA
	R: ATGGTGACACAGTTACTCGGT
SMAD5	**F:** CCAGCAGTAAAGCGATTGTTGG
	R: GGGGTAAGCCTTTTCTGTGAG
ACVRL1	**F:** CATCGCCTCAGACATGACCTC
	R: GTTTGCCCTGTGTACCGAAGA
KLF2	**F:** TTCGGTCTCTTCGACGACG
	R: TGCGAACTCTTGGTGTAGGTC
ETS1	**F:** GATAGTTGTGATCGCCTCACC
	R: GTCCTCTGAGTCGAAGCTGTC

Table S2: List of antibodies used in immunocytochemistry (related to figures 1, 4, S1, S3)

Primary antibody	**Source**	**Identifier**	**Host**	**Concentration**
Anti-WT1	Abcam	ab89901	Rabbit	1:50
Anti-TBX18	Abcam	ab115262	Rabbit	1:50
Anti-ZO-1	Invitrogen	ZO1-1A12	Mouse	1:200
Anti-CD105/Endoglin (D50G1)	CST	#4335	Rabbit	1:200
Anti-NG2/CSPG4	CST	#52635	Rabbit	1:200
Anti-SMAD3	Abcam	ab40854	Rabbit	1:500
Anti-phospho-SMAD3	Abcam	ab52903	Rabbit	1:100
Secondary antibody				
Anti-rabbit IgG-Alexa Fluor 647	Life Technologies	A21245	Goat	1:1000
Anti-mouse IgG-Alexa Fluor 488	Life Technologies	A11001	Goat	1:1000

Table S3: List of antibodies used in flow cytometry (related to figures 1, 3, 4, 5, 6, S5, S6)

Primary antibody	**Source**	**Identifier**	**Host**	**Concentration**
Anti-WT1	Abcam	ab89901	Rabbit	1:100
Anti-TBX18	Abcam	ab115262	Rabbit	1:100
Anti-cTnT	Thermo Scientific	MS295P	Mouse	1:100
Secondary antibody				
Anti-rabbit IgG-Alexa Fluor 647	Life Technologies	A21245	Goat	1:1000
Anti-mouse IgG-Alexa Fluor 488	Life Technologies	A11001	Goat	1:1000
Conjugated antibody				
CD105-APC	BD	562408	Mouse	1:100
NG2-Alexa Fluor 647	BD	562414	Mouse	1:100
CD44-PE	BD	550989	Mouse	1:100

Table S4: List of antibodies used in western blotting (Simple Western) (related to figures 1, 2, 3, 4, 6, S1, S3, S4, S5)

Primary antibody	**Source**	**Identifier**	**Host**	**Concentration**
Anti-β-actin	Sigma-Aldrich	A5441	Mouse	1:100
Anti-WT1	Abcam	ab89901	Rabbit	1:20
Anti-TBX18	Abcam	ab115262	Rabbit	1:20
Anti-SMAD3	Abcam	ab40854	Rabbit	1:20
Anti-phospho-SMAD3	Abcam	ab52903	Rabbit	1:20
Anti-α-SMA	Abcam	ab7817	Mouse	1:20
Anti-TAGLN	CST	#40471	Rabbit	1:20
Anti-CNN1	CST	#17819	Rabbit	1:20
Anti-CD105/Endoglin (D50G1)	CST	#4335	Rabbit	1:20
Anti-NG2/CSPG4	CST	#52635	Rabbit	1:20
Anti-CD248	CST	#47948	Rabbit	1:20
Anti-CD13	Abcam	ab108310	Rabbit	1:20
Anti-CDK4	CST	12790	Rabbit	1:20
Anti-CDK6	CST	13331	Rabbit	1:20
Anti-TNNI1	Abcam	203515	Rabbit	1:20
Anti-SMAD2	CST	#5339	Rabbit	1:20
Anti-phospho-SMAD2	CST	#3108	Rabbit	1:20
Anti-SMAD2/3	CST	#3102	Rabbit	1:20
Anti-phospho-SMAD2/3	CST	#8828	Rabbit	1:20
Anti-ID1	CST	#23369	Rabbit	1:20
Anti-ID3	CST	#9837	Rabbit	1:20
Anti-KLF2	CST	#15306	Rabbit	1:20
Anti-SMAD1	CST	#6944	Rabbit	1:20
Anti-phospho-SMAD1/5/9	CST	#13820	Rabbit	1:20
Secondary antibody				
Anti-Rabbit Secondary HRP Antibody	Bio-Techne	042-206	Goat	1:1
Anti-Mouse Secondary HRP Antibody	Bio-Techne	042-205	Goat	1:1

Table S5: List of ELISA kits (related to figures 6, S6)

Name	Source	Identifier
Human VEGFA ELISA Kit	Abcam	ab119566
Human Angiopoietin 1 ELISA Kit (ANG1)	Abcam	ab99972
Human SDF1 alpha ELISA Kit	Abcam	ab100637

Supplemental experimental procedures

Epicardial differentiation

For epicardial differentiation, on day 0, iPSCs were dissociated using Accumax and embryoid bodies (EBs) were generated in HEMA-coated plates (6000 cells/well, for 96-well plate). We used 70 µl/well of the following differentiation media on day 0: StemPro®-34 media supplemented with 2 mM L-glutamine, 50 µg/ml ascorbic acid (AA), 0.4 µM monothioglycerol (MTG), 150 µg/ml transferrin, 10 µM Y-27632, 2 ng/ml rh BMP4 and 0.5% Matrigel. After 24 hours, we added more 70 µl/well media to obtain the following final concentration: 2 mM L-glutamine, 50 µg/ml AA, 0.4 µM MTG, 150 µg/ml transferrin, 10 µM Y-27632, 10 ng/ml rh BMP4, 2 ng/ml Activin A and 5 ng/ml rh bFGF. On day 3.5, EBs were collected and dissociated using Accumax, subsequently plated onto 0.1% gelatin-coated dishes (0.25×10^5 cells/cm^2), suspended in the following differentiation media: StemPro®-34 media supplemented with 2 mM L-glutamine, 50 µg/ml AA, 0.4 µM MTG, 150 µg/ml transferrin, 10 µM Y-27632, 3 mM CHIR99021, 30 ng/ml rh BMP4, 5 ng/ml rh VEGF and 10 µM SB431542. On day 6, the media was changed with the same media on day 3.5 only without Y-27632. On day 8, hiPSC-derived epicardial cells were maintained in the following maintenance media: DMEM high glucose containing 10% FBS and 10 µM SB431542. EPI cells were detached by Accumax, dissociated, and replated as described above not to be too confluent, approximately every 5 days.

Cardiomyocyte differentiation

For cardiomyocytes differentiation, the protocol is same for epicardial differentiation on day 0, except that the cell number is 2 million/well for 6-well plate and the amount of the media is 1.5 ml/well. On day 1, we added more 1.5ml/well media to get the following final concentration (induction media 1): 2 mM L-glutamine, 50 µg/ml AA, 0.4 µM MTG, 150 µg/ml transferrin, 10 µM Y-27632, 10 ng/ml rh BMP4, 6 ng/ml Activin A and 5 ng/ml rh bFGF. On day 3, EBs were washed by IMDM and suspended in the following media (induction media 2): StemPro®-34 media supplemented with 2 mM L-glutamine, 50 µg/ml AA, 0.4 µM MTG, 150 µg/ml transferrin, 10 ng/ml rh VEGF and 1 µM IWP-3. On day 7, the media were changed to the following media

(induction media 3): StemPro®-34 media supplemented with 2 mM L-glutamine, 50 µg/ml AA, 0.4 µM MTG, 150 µg/ml transferrin and 5 ng/ml rh VEGF. After that, media change was performed with the induction media 3 every 2-3 days until day 16. On day 16, cells were detached by collagenase I and Accumax and plated onto fibronectin-coated dishes (1.0×10^5 cells/cm^2), suspended in the induction media 3. After that, media change with the induction media 3 was performed every 2-3 days until day 23.

Cardiac fibroblasts and Smooth muscle cells differentiation (EMT induction)

For differentiation towards CF, EPI cells at day 24 were treated with 10 ng/ml bFGF for 8 days. For differentiation towards SMC, EPI cells at day 24 were treated with 5 ng/ml TGF-β for 4 days followed by 10 ng/ml bFGF for another 4 days.

Endothelial Tube Formation assay (*in vitro* Angiogenesis)

For the endothelial tube formation assay, we first added 35 µl of Matrigel to each well of a pre-chilled 96-well plate and incubated it for 1 hour at 37ºC. After incubation, a cell suspension (totaling 3.0×10^4 cells per 150 µl) was added to each well and then incubated at 37ºC. In co-culture experiments, we utilized Human Aortic Endothelial Cells (HAEC) along with only the EGFP-positive population in EGFP-overexpressed iPSC-derived epicardial cells (EPI cells). The cell suspension was prepared by mixing them in a 1:1 ratio. Images were acquired 4 to 12 hours after starting the assay. Tube formation was quantified by counting the number of junctions in a rectangle measuring 3623.44 µm in length and 2717.58 µm in width using ImageJ.

Assessment of paracrine signaling by SMAD3-downregulating cells on the proliferative activity of hiPSC-derived cardiomyocytes.

FUCCI-expressing hiPSCs were differentiated into cardiomyocytes as described previously. On day 23, the cardiomyocytes were cultured for 36 hours in supernatants from either SMAD3-silenced or control EPI cells. These supernatants were collected 7 days post-siRNA transfection. In this experiment, the media was changed only once, 24 hours after siRNA transfection, and SB431542 was added to the media every few days thereafter.

Image acquisition, processing, and analysis

Microscopy images were taken by BZ-X710 and BZ-X 810 (Keyence). A representative section was chosen, cropped and magnified for phase contrast and fluorescence pictures. For counting the number of junctions in endothelial tube formation assay, navigation mode was used. General image analysis was performed using Microsoft power point as well as ImageJ v1.54d.

Real-time quantitative PCR analysis

Live cells were collected in QIAzol lysis reagent. Total RNA was purified using the RNAeasy Micro Kit (Qiagen) according to the provided protocol. Complementary DNA was synthesized using the ReverTra Ace system (Toyobo BIOTECH) according to the manufacturer's manual. Quantitative RT-PCR was performed using THUNDERBIRD™ Next SYBR® qPCR mix with primers (summarized in Table S1). Data acquisition was carried out by QuantStudio™ 3 Real-Time PCR System (Applied Biosystems™). All data were acquired from at least three biological replicates and analyzed using Microsoft Excel and GraphPad Prism v9. The relative mRNA expression was normalized to GAPDH and calculated using the relative fold change ($2^{-\Delta\Delta CT}$) in each gene.

We excluded values that lacked any recorded data. When dealing with datasets that displayed a normal distribution, we performed a Student's t-test, as specified in the figure legends. All error bars in our graphs represent the standard error of the mean (SEM).

Immunocytochemistry

Cells were fixed with 4% paraformaldehyde for 30 min at room temperature and stored in PBS at 4ºC. Blocking was performed for 30 min in blocking buffer: 1% BSA, 0.5% Triton X and 0.1M glycine in PBS. Following PBS washing, primary antibody was added in staining buffer (blocking buffer without glycine) and incubated overnight at 4ºC. After incubation and PBS washing, secondary antibody was added in staining buffer and incubated for 2 hours at 4ºC. After incubation and PBS washing, Hoechst (Life Technologies; H3570, 1:10000) was added for nuclear counterstaining. The information of used antibodies and concentrations were shown in Table S2.

Flow cytometry analysis/FACS

Cells were dissociated by Accumax, washed twice, and fixed with 4% paraformaldehyde for 30 min at room temperature. In case for nuclear staining, following PBS washing, the cells were permeabilized by 90% methanol for 30min at 4 ºC. After permeabilization and PBS washing, primary antibody was diluted in FACS Buffer (10% FBS in PBS) and incubated overnight at 4ºC. The next day, following PBS washing, secondary antibody was added in FACS Buffer and incubated for 2 hours at 4ºC. In case for cell surface marker staining, following PBS washing, conjugated antibody was diluted in FACS buffer and incubated at room temperature for 30 min. Stained cells were analyzed and sorted using FACSAria II (BD Biosciences). Data were analyzed using FlowJo v10.6.1 analysis software (BD Biosciences). The information of used antibodies and concentrations were shown in Table S3.

We identified the cell population by using FSC/SSC gating, and we distinguished doublets based on the method explained in Figure S6e. To establish the negative gates, we utilized unstained samples or isotype controls, and we also included negative control samples in our analysis.

Western blotting (Simple Western)

Cells were detached and collected in Mammalian Protein Extraction Reagent (M-PER) (Thermo Scientific; 78501). The amount of protein was determined by using Quick Start™ Bradford Protein Assay (Bio-Rad) and EnVision 2104 plate reader (Perkin Elmer) as the standard. We used a Wes™ instrument (ProteinSimple) as protocol instructed. The information of used antibodies and concentrations were shown in Table S4. The chemiluminescence of protein was quantified using Compass for SW software v6.2.0 (ProteinSimple), although WT1, CD105, and CDK6 were difficult to quantify because of the problems with sensitivity of the antibody.

Enzyme-linked immunosorbent assay (ELISA)

The levels of VEGFA, SDF-1, and ANG1 were assessed using ELISA kits shown in Table S5, following the manufacturer's manual. Absorbance at 450 nm was measured using EnVision 2104 plate reader (Perkin Elmer).